Progress in Particle and Nuclear Physics 62 (2009) 102–134

Contents lists available at ScienceDirect

Progress in Particle and Nuclear Physics

journal homepage: www.elsevier.com/locate/ppnp

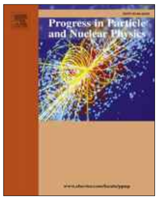

Review

Torsion balance experiments: A low-energy frontier of particle physics

E.G. Adelberger*, J.H. Gundlach, B.R. Heckel, S. Hoedl, S. Schlamminger

Center for Experimental Nuclear Physics and Astrophysics, Box 354290, University of Washington, Seattle, WA 98195-4290, USA

A R T I C L E   I N F O

Keywords:
Torsion balance
Equivalence principle
Inverse square law
Lorentz invariance

A B S T R A C T

We review recent mechanical experiments that test some of the most basic principles of physics including the weak and strong forms of the Equivalence Principle, the gravitational inverse-square law, and Lorentz invariance. The very high sensitivity of these tests allows one to place interesting constraints on string-theory inspired conjectures about new Yukawa forces from the exchange of very light scalar, pseudoscalar or vector particles, large extra dimensions, the chameleon mechanism, non-commutative spacetime geometry, and Planck-scale Lorentz violation.

Contents

---

* Corresponding author.
E-mail address: eric@npl.washington.edu (E.G. Adelberger).

0146-6410/$ – see front matter © 2008 Published by Elsevier B.V.
doi:10.1016/j.ppnp.2008.08.002

1. Introduction

It is a very remarkable thing that gravitation, a subject that began with Newton, and "gravitational" experiments using torsion balances, a subject that began with Cavendish, are both still relevant to some of the most profound questions in fundamental physics. After all, we have a very successful classical relativistic theory of gravity (General Relativity) that has passed all experimental tests to date, and a very successful quantum gauge theory (the Standard Model) that also accounts (with some modifications to account for neutrino masses and mixing) for all experiments in particle physics. What then is the problem? It is that the two theories are fundamentally incompatible. Physicists are therefore devoting an intense effort to find a single framework that unifies *all* the fundamental forces of nature. Furthermore astrophysical observations have shown that the stuff of the Standard Model accounts for only 4% of the mass and energy of the entire Universe and that the majority consists of a mysterious "dark energy" [1]. These two considerations have driven theoretical work that motivates much of the experimental work that is the subject of this review. A large part of theoretical speculation is based on ideas from string theory which, at this moment, is the only known framework for unifying gravity with the rest of physics. However this theory inherently contains features that have to be hidden from experiment–extra dimensions and many nominally massless scalar particles called moduli. Both of these features may, in principle, show up as novel effects in the kind of gravitational experiments we discuss. Much of this is discussed in a detailed 2003 review by some of us [2]; this article concentrates on developments since 2003. Our selection of experimental topics naturally reflects the research agenda of the University of Washington Eöt–Wash group, to which we all belong.

2. Tests of the equivalence principle

2.1. Motivation

The Equivalence Principle (EP) states that a homogeneous gravitational field is locally equivalent to a uniformly accelerated reference frame (or equivalently that in freely falling frames all local effects of gravity disappear exactly). This principle was the central inspiration that led Einstein to develop General Relativity, his relativistic theory of gravity that explained gravity, not as a conventional force, but rather as the result of an object following a geodesic in curved space time. The most direct, and most precisely tested, prediction of the EP is the Universality of Free Fall (UFF): *i.e.* that the trajectory of a point object freely falling in a gravitational field depends only on the object's initial condition and not on its composition.

The EP can be understood in Newtonian terms as requiring the exact identity of m_i and m_g, the inertial and gravitational masses of any body. For many years EP tests were conceived of in exactly these terms: is m_i exactly equal to m_g? Because the mass of any body is a sum of the energies of its constituents and their mutual interactions, a composition dependence of the free fall acceleration would arise if any of the ingredients of a body's mass contributed differently to m_g and m_i. The figure of merit for any UFF test is the degree to which the test bodies are different divided by by the precision of the differential acceleration measurement. The relevant test-body differences are the proton-to-neutron ratios, and the fractional contributions to the test body masses of the binding energies due to the gravitational, weak, electromagnetic and strong interactions. It is customary to distinguish two forms of the EP, the Weak EP which states that all interactions, except for gravity, give equal contribution to m_i and m_g, and the Strong EP which applies to gravity as well. Laboratory tests of the UFF have reached a precision that confirms the Weak EP with high significance, but clearly such tests cannot test the Strong EP because gravitational binding energy is negligible for laboratory-sized bodies. (The gravitational binding energy scales like the mass of the body squared and for a body as large as the Earth amounts to only 0.5 μg/kg.) Nevertheless, torsion balance experiments play a role in tests of the strong equivalence principle. As discussed at the end of this section, torsion balance results can complement lunar laser ranging data to provide a loop-hole free test of the strong EP.

Because General Relativity has passed all experimental tests–for example, null results from EP tests reach a precision of $\Delta a/a \sim 2 \times 10^{-13}$ (see below), the time delay of photons passing through the vicinity of the Sun agrees with the theory to 2 parts in 10^5 [3], and the Hulse–Taylor binary-pulsar provides a precise test of many aspects of strong-field gravity, including a 0.2% measurement of the gravitational radiation reaction [4] — it is reasonable to view EP tests in a more general light. In addition to testing General Relativity ever more precisely, one can adopt the working assumption that classical gravity obeys the EP exactly, and view the tests instead as broad-gauge and extraordinarily sensitive probes for new, ultra-feeble vector or scalar interactions. To our knowledge, Lee and Yang were the first to do this, speculating that the apparent conservation of baryon number, B, might be accompanied by a massless vector field coupled to B, and used existing EP data to test this hypothesis [5]. There are now many suggestions that such interactions may exist, and string or M-theory has been particularly fruitful in this regard (see Ref. [2] for a detailed account). For example, the theory requires a large number of initially massless scalar particles with nominally "gravitational" strength couplings: the scalar partner of the spin-2 graviton called the dilaton as well as many so-called moduli, all of which would mediate "gravitational strength" EP-violating exchange forces.

Scalar or vector interactions violate the EP because they couple to "charges" and not to mass, producing static potentials between point objects of the form

$$\tilde{V}_{1A}(r) = \mp \frac{1}{4\pi} \tilde{q}_1 \tilde{q}_A \frac{\mathrm{e}^{-r/\lambda}}{r}, \tag{1}$$

where $\tilde{q}_A$ and $\tilde{q}_1$ are the scalar or vector "charges" of the attractor and the test body respectively. The interaction range is given by the Compton wavelength $\lambda = \hbar/m_b c$ of the exchanged boson. The upper$(-)$ and lower$(+)$ signs apply to scalar and vector interactions, respectively. For electrically neutral bodies consisting of atoms with charge and neutron numbers Z and N, the "charge" can be written as

$$\tilde{q} = \tilde{g}[Z \cos \tilde{\psi} + N \sin \tilde{\psi}] \tag{2}$$

where $\tilde{g}$ is a coupling constant and $\tilde{\psi}$ (which in principle can have any value between $-\pi/2$ and $\pi/2$) is a parameter that specifies the details of the charges

$$\tan \tilde{\psi} \equiv \frac{\tilde{q}_n}{\tilde{q}_e + \tilde{q}_p}. \tag{3}$$

For example an interaction coupled to B ($\tilde{q}_p = \tilde{q}_n = \tilde{g}$, $\tilde{q}_e = 0$) corresponds to $\tilde{\psi} = \pi/4$, while $\tilde{\psi} = 0$ corresponds to a coupling to lepton number L. An interaction coupled to $B - L$ is especially interesting because in Grand Unified Theories $B - L$ is conserved although B and L are not conserved individually. In this case, the charges are $\tilde{q}_p = \tilde{q}_n = \tilde{g}$ and $\tilde{q}_e = -\tilde{g}$, which corresponds to $\tilde{\psi} = \pm\pi/2$.

The Yukawa acceleration of body 1 toward an attractor A is

$$\boldsymbol{a}_1 = -\frac{\nabla \tilde{V}}{m_1} = \mp \frac{\tilde{q}_1}{m_1} \frac{\tilde{q}_A}{4\pi} \left(\frac{1}{r^2} + \frac{1}{r\lambda} \right) \mathrm{e}^{-r/\lambda} \hat{\boldsymbol{r}}, \tag{4}$$

which is proportional to the "charge" to mass ratio of the body. Unless $\tilde{q}/m$ is identical for all objects, the acceleration induced by scalar or vector boson exchange will apparently violate the EP. It is easy to see that any vector interaction must violate the EP, because a particle and its antiparticle have opposite vector charges. Vector charges are Lorentz scalars and conserved, so that an object's $\tilde{q}$ is the sum of the $\tilde{q}$'s of its constituents. However, the object's mass is less than the mass of its constituents because of binding energy. The situation for scalar charges is more complex–scalar charges are not conserved (the *charge density* is a Lorentz scalar, not the charge itself) and binding energy can carry scalar charge–but again one expects that a scalar interaction coupling to the elementary fermions will appear to violate the EP [6].

Eq. (1) can be re-expressed in a form that makes manifest its connection to EP experiments

$$V(r) = -G \frac{m_1 m_2}{r} \left(1 + \tilde{\alpha} \left[\frac{\tilde{q}}{\tilde{g}\mu} \right]_1 \left[\frac{\tilde{q}}{\tilde{g}\mu} \right]_2 \mathrm{e}^{-r/\lambda} \right), \tag{5}$$

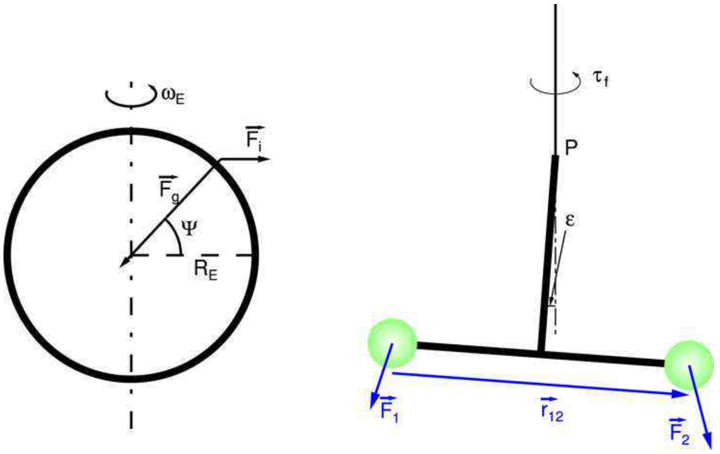

Fig. 1. The left graph shows the inertial and gravitational forces on a test-body mounted at a latitude $\Psi = 47°$. The ratio of the forces is exaggerated by a factor 200. The right figure shows the forces on a simplified torsion pendulum where m_2 is greater than m_1. The pendulum tips by an angle ϵ so that the center of mass lies vertically below P.

where μ is a test body mass in units of atomic mass unit u, and

$$\tilde{\alpha} = \pm\tilde{g}^2/(4\pi G u^2). \tag{6}$$

In this notation, the differential Yukawa acceleration of bodies 1 and 2 toward an attractor A is

$$\frac{\Delta a}{g} = -\tilde{\alpha}\left(\Delta\left[\frac{Z}{\mu}\right]\cos\tilde{\psi} + \Delta\left[\frac{N}{\mu}\right]\sin\tilde{\psi}\right)\left(\left[\frac{Z}{\mu}\right]_A\cos\tilde{\psi} + \left[\frac{N}{\mu}\right]_A\sin\tilde{\psi}\right)\left(1+\frac{r}{\lambda}\right)e^{-r/\lambda}, \tag{7}$$

where the first term in large curved brackets refers to the difference in the properties of test bodies 1 and 2. Note that there are always two values of $\tilde{\psi}$, $\tilde{\psi}^0_{tb}$ and $\tilde{\psi}^0_A$, for which any test-body pair/attractor combination will have have no sensitivity, because either the difference in the "charge"-to-mass ratio of test-body pair or the attractor "charge" vanishes. Hence a broad search for new Yukawa interactions requires at least two different test-body composition dipoles and two different attractor materials; furthermore, to have sensitivity for short λ's the search must employ attractors that are as close to the torsion balance as consistent with a significant signal.

2.2. *Experimental issues*

2.2.1. *Basic principles*

Fig. 1 shows a simplified sketch of an EP torsion balance. The fiber defines the local vertical for a particular pair of test-body materials. Clearly, the torsion balance is only sensitive to the differential acceleration in the local horizontal plane. The fiber direction is $\hat{\boldsymbol{n}} = -(\boldsymbol{F}_1 + \boldsymbol{F}_2)/|\boldsymbol{F}_1 + \boldsymbol{F}_2|$ and the magnitude of the torque along the fiber is [7]

$$\tau = \frac{(\boldsymbol{F}_1 \times \boldsymbol{F}_2)\cdot \boldsymbol{r}_{12}}{|\boldsymbol{F}_1 + \boldsymbol{F}_2|}, \tag{8}$$

which vanishes if $\boldsymbol{F}_1$ and $\boldsymbol{F}_2$ are parallel. In the absence of stray forces, a non-zero torque can occur for only two reasons: the EP is violated so that local vertical (defined by the superpositions of the gravitational and inertial forces) differs for the two materials, or because the two test bodies are in different locations in a nonuniform gravitational field. If the force vectors on the two test bodies are not parallel, a torque acts on the pendulum which causes it to twist until the fiber's restoring torque, $-\kappa\theta$, counteracts the original torque. The pendulum's twist can be monitored by reflecting a collimated light beam from a small mirror mounted on the pendulum. One then can infer, if the ambient gravitational field is sufficiently uniform, that

$$-\kappa\theta = \Delta a_\perp \frac{m_1 m_2}{m_1 + m_2} r_{12}\cos\epsilon \tag{9}$$

where $\Delta a_\perp$ is the horizontal component of the differential test body acceleration. In practice, the test bodies have very similar masses, m, and moment arms, r, so that Eq. (9) leads to

$$\Delta a_\perp = -2\frac{\kappa\theta}{m r_{12}}. \tag{10}$$

The pendulum's equilibrium orientation is arbitrary, as it depends on how the upper end of the fiber is mounted. To obtain a meaningful result one must rotate the pendulum (or attractor) by 180 deg and measure the correlated *change* in θ.

Table 1
The Z/μ, N/μ and B/μ ratios of test-body materials of particular interest in EP tests, weighted by the isotopic abundances when applicable

Material	ρ (g/cm^3)	Z/μ	N/μ	B/μ
Be	1.9	0.44384	0.55480	0.99865
PE	1.0	0.57034	0.42854	0.99888
MM	2.1	0.49813	0.50250	1.00063
Al	2.7	0.48181	0.51887	1.00068
Ti	4.5	0.45961	0.54147	1.00108
EC	7.7	0.46610	0.53504	1.00114
Cu	9.0	0.45636	0.54475	1.00112
Pt	21.4	0.39984	0.60034	1.00018
Au	19.3	0.40108	0.59909	1.00017
Pb	11.3	0.39572	0.60440	1.00012

PE denotes ultra-high molecular weight polyethylene. MM and EC were test bodies used in an experiment [8] related to the Strong EP test; MM is a test body simulating the very similar compositions of the Moon and the Earth's mantle, and EC a test body with a composition similar to the Earth's core.

Table 2
Charge to mass ratio differences for some test-body pairs

($\times 10^{-2}$)	Be	PE	Al	Ti	Cu	Pt	Au
Be		−12.65	−3.80	−1.58	−1.25	4.40	4.28
PE	−12.63		8.85	11.07	11.40	17.05	16.93
Al	−3.59	9.03		2.22	2.54	8.20	8.07
Ti	−1.33	11.29	2.26		0.32	5.98	5.85
Cu	−1.01	11.62	2.59	0.33		5.65	5.53
Pt	4.55	17.18	8.15	5.89	5.56		−0.12
Au	4.43	17.05	8.02	5.76	5.43	−0.13	

The numbers above the diagonal give $\Delta[Z/\mu]$, numbers below the diagonal give $\Delta[N/\mu]$. Large values lead to high sensitivity.

Table 3
Inherent sensitivity to B-coupled interactions of the test-body pairs in Table 2

	Be	PE	Al	Ti	Cu	Pt	Au
Be		45.1	46.6	49.8	51.2	44.0	44.0
PE	0.2		44.4	44.4	44.4	44.8	44.8
Al	2.0	−1.8		44.5	44.5	45.2	45.2
Ti	2.4	−2.2	−0.4		44.7	45.4	45.4
Cu	2.5	−2.2	−0.4	0.0		45.5	45.5
Pt	−1.5	−1.3	0.5	0.9	0.9		44.7
Au	−1.5	−1.3	0.5	0.9	0.9	0.0	

Numbers below the diagonal give $\Delta[B/\mu][B/\mu]_A \times 10^3$; numbers above the diagonal show $\tilde{\psi}^0_{tb}$ in degrees.

This idea was originally implemented by Lorand Eötvös, who also introduced the Eötvös parameter η that quantifies EP tests

$$\eta \equiv \frac{\Delta a_\perp}{g_\perp}, \tag{11}$$

where $g_\perp$ is the horizontal component of the gravitational acceleration. At a latitude of 45° $g_\perp = 1.7$ cm/s^2.

A torsion balance is able to compare test body accelerations with precisions of parts in 10^{13} although the dimensions and masses on the pendulum are only good to parts in 10^4 because the EP torsion pendulum is an exquisitely sensitive null instrument for comparing the *angles* (rather than the magnitudes) of the force vectors on two bodies.

2.2.2. Choice of test-body materials

For obvious reasons, EP test masses are restricted to non-magnetic, conducting solids. Table 1 shows the $[N/\mu]$, $[Z/\mu]$ and $[B/\mu]$ ratios for some useful materials. Note the very small variation in B/μ values, which reflects the relatively small contribution of binding energy to the mass of an atom. Therefore it is a good approximation that all attractors have $[B/\mu]_A = 1$. Table 2 gives the differences $\Delta[Z/\mu]$ and $\Delta[N/\mu]$ of some test-body pairs made from the materials in Table 1. Table 3 shows the sensitivity of various test-body pairs to an interaction coupled to B.

2.2.3. Choice of attractors

Because the charge of a single attractor vanishes at $\tilde{\psi}_0 = \arctan(-Z/N)$, limits on the complete parameter space for $\tilde{\psi}$ can only be set by employing multiple attractors with different compositions. Table 4 compares attractors used by the Eöt–Wash group.

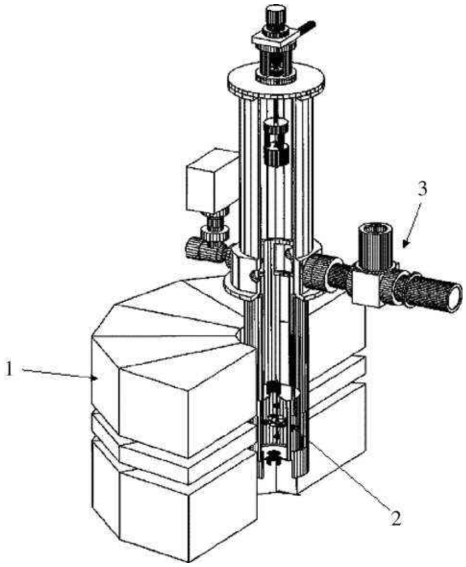

Fig. 2. Simplified view of the apparatus used in the EP test by Smith et al. [10]. An autocollimator(3) detected the pendulum twist as a three-ton depleted uranium attractor(1) was rotated about the torsion pendulum(2). The attractor shape was designed to minimize gravitational couplings. A 1 ton attractor counterbalance (not shown) located 3 times farther from the pendulum eliminated systematic errors from floor tilt. The relative angle of the 3 attractor components could be changed to map out the sensitivity of the pendulum to low order-gradients. This experiment was designed to be particularly sensitive to a charge $N - Z$ for which experiments using the earth crust are relatively insensitive.

Table 4
Properties of attractors used in EP tests of Refs. [10,11], with the approximate distance to the source in the second column

Attractor	R_A (m)	Z/μ	N/μ	B/μ	$\tilde{\psi}_A^0$ (deg)	$g_\perp^{\max}$ (m/s^2)	
Depleted uranium	1	0.39	0.61	1.00	−32	9.2×10^{-7}	
Local topography	$5 - 2 \times 10^4$	0.50	0.50	1.00	−55	7.2×10^{-5}	
Entire earth	5×10^7	0.49	0.51	1.00	−44	1.7×10^{-2}	Ref. [14]
Sun	2×10^{11}	0.86	0.14	0.99	−81	5.9×10^{-3}	
Galaxy	3×10^{20}					1.9×10^{-10}	
Galactic DM	3×10^{20}					4.8×10^{-11}	Ref. [15]

The second to last column shows the maximum perpendicular gravitational acceleration caused by this attractor.

For interaction ranges λ between ≈0.1 and ≈5 m, good constraints can be obtained using well-characterized materials placed in the vicinity of the torsion balance. In this case a modulated EP signal can be obtained by rotating the attractor around a stationary balance. The EP experiments of Nelson et al. [9] and Smith et al. [10] are examples of this technique. Fig. 2 shows the apparatus of Ref. [10].

For longer ranges λ, the Earth is an effective attractor. However, on a perfectly leveled Earth, for example at sea, the local horizon is perpendicular to the sum of the gravitational and inertial forces so that an interaction with λ small compared with the size of the Earth cannot twist a pendulum as it produces vertical forces on the test bodies. To investigate such forces one must take advantage of local topographic features (such as a hill) that can produce horizontal accelerations. The source strength as a function of λ is calculated by integrating Eq. (4) over the local topography. The acceleration perpendicular to local vertical determines the sensitivity of the experiment, and depends strongly on the specific site. For ranges $\lambda > 10^6$ m, the Earth as a whole provides the major contribution to the source strength. The source strength increases monotonically until $\lambda \approx 5 \times 10^7$ m, at which point the whole Earth contributes to the integral.

To obtain a modulated signal from the terrestrial attractor, the torsion balance must be placed on a turntable that rotates either continuously or in discrete steps. Most stochastic noise sources have a spectral density that rises sharply at low frequencies, so that the ability to modulate the signal at frequencies comparable to the pendulum's free-oscillation frequency is a significant advantage. The continuous rotation scheme used in the Eöt–Wash experiments [11,12] has the advantage that the pendulum fiber is essentially untwisted by the rotation. However, the rotation rate must be extremely uniform to avoid generating false signals or excess noise. Newman has rotated a torsion balance instrument in discrete steps, which avoids issues with the constancy of the rotation rate. However, to avoid a large twist in the torsion fiber during changes in the apparatus' orientation, the pendulum was co-moved with an eddy current generating magnetic field so that it would follow the turntable [13].

The Sun provides an excellent attractor for probing interactions with $\lambda \geq 1.5 \times 10^{11}$ m. Because its apparent position changes with a 24 h period, the modulation of the signal is effortless; however many systematic errors, such as temperature variations, building tilt and vibrations from human activity, occur at this same period. The Sun's composition, 71% of its mass is H and 27.1% He, gives a value of ψ_0 very different from the other attractors that can be exploited to yield stronger constraints as discussed below.

At ranges $\lambda \geq 2 \times 10^{20}$ m the center of the Milky Way provides an attractor that includes a significant amount of dark matter (DM); it is expected that about a quarter of the solar system's acceleration towards the center of the galaxy is caused by dark matter [15]. Remarkably, torsion balance experiments are sensitive to differential accelerations of normal matter to DM at the $10^{-5}g_{\mathrm{DM}}$ level. The natural modulation period of this source is a sidereal day, so that any ambiguity of the acceleration towards the solar and galactic attractors can easily be resolved by a year long measurement; after half a year the phase between the two signals has changed by 180°.

2.2.4. *False effects from gravity gradients*

A fundamental limitation in EP experiments is the sensitivity of the torsion pendulum to gravity gradients. The gravitational torque about the torsion fiber as a function of the angle, ϕ, between the pendulum and attractor can be expressed by an expansion in spherical multipole moments [7,11],

$$\tau(\phi) = 8\pi G \sum_{l=0}^{\infty} \frac{1}{2l+1} \sum_{m=-l}^{l} m \, \mathrm{Im}[q_{lm} Q_{lm} \mathrm{e}^{-\mathrm{i}m\phi}], \tag{12}$$

where the outer mass moments Q_{lm} describe the ambient gravity gradients

$$Q_{lm} = \int \rho_A(\mathbf{r}) r^{-(l+1)} Y_{lm}(\hat{\mathbf{r}}) \mathrm{d}^3\mathbf{r}, \tag{13}$$

and the q_{lm} are the body-fixed inner mass moments of the pendulum about its center of mass

$$q_{lm} = \int \rho_P(\mathbf{r}) r^l Y^*_{lm}(\hat{\mathbf{r}}) \mathrm{d}^3\mathbf{r}. \tag{14}$$

Since the EP signal occurs at the frequency with which the pendulum or the source is rotated, the terms with $m = 1$ will produce a false effect. Note that for a freely hanging pendulum suspended from a flexible fiber, the q_{11} moment vanishes. This condition is essential for the functioning of a torsion balance. The torque sum converges rapidly as $(r_P/R_A)^l$, with r_P and R_A being the typical dimensions of the pendulum and the distance to the attractor.

For experiments designed to have sensitivity to ranges up to 10^6 m, careful attention must be paid to minimizing low-order $m = 1$ gravitational couplings. This is done by designing pendulums with negligible $m = 1$ inner moments (see Ref. [16] for computational methods) and by measuring the ambient gravity gradients and installing suitably shaped compensators that null the dominant gravity gradients.

2.3. *Experimental results*

2.3.1. *The classic experiments*

Loránd Eötvös and collaborators were the first to use a torsion balance to test the equivalence principle [17]. Their best results came studying the differential accelerations of a wide variety of test-body pairs in the field of the Earth. This required that the apparatus be rotated by 180 degrees to obtain a meaningful signal. For example, they found $\eta_{\oplus}(\mathrm{Cu}, \mathrm{Pt}) = (4 \pm 2) \times 10^{-9}$. To appreciate this achievement it should be noted that previous experiments with simple pendulums attained a precision of only $\approx 10^{-5}$ [18]. Eötvös et al. also studied differential accelerations toward the Sun, so that the Earth's rotation provided a periodic modulation of the EP signal without disturbing the apparatus. However, those results were not competitive with their Earth-based test.

The next major advance was made by Roll, Krotov and Dicke [19] whose EP test using the Sun as an attractor introduced the electrostatic torque-feedback scheme discussed in Section 6. Dicke and coworkers employed Au and Al test bodies and obtained $\eta_{\odot}(\mathrm{Au}, \mathrm{Al}) = (1.3 \pm 1.5) \times 10^{-11}$ (we have converted the probable error given in [19] to a standard deviation). Despite the fact that the $g_{\perp}$ to the Sun is 2.9 times lower than $g_{\perp}$ to the Earth, this result was two orders of magnitude more precise than that of Eötvös et al. This was made possible by the smooth modulation provided by the Earth's rotation, the longer integration time, and the negligible role of false effects from gravity gradients. Roll, Krotov and Dicke also reported a less sensitive measurement using Cu and PbCl_2 as test bodies. Subsequently, Braginsky and Panov [20] did an EP experiment with the solar attractor and a free (no torque feedback) torsion pendulum containing multiple Al and Pt test bodies. They reported $\eta_{\odot}(\mathrm{Al}, \mathrm{Pt}) = (3 \pm 4) \times 10^{-13}$. This higher sensitivity was achieved by a fiber with a smaller torsional constant and a larger lever arm. However, the diurnal signals of the solar experiments had to contend with a number of possible systematic effects (temperatures, etc.) that also occur at a daily frequency.

2.3.2. *The "fifth force" era*

After the completion of the classic experiments, little further activity took place until 1986 when Fischbach et al. [21] reanalysed the Eötvös data. They used this, along with previous claims of anomalous data on g in mines [22], to claim evidence for a new force. This "fifth force" was an EP-violating acceleration coupled to B with a range of a few hundred meters that would have rendered it invisible to the classic solar EP tests. This finding triggered many experiments looking for intermediate-range ($10 \text{ m} < \lambda < 10000$ km) forces. The Eöt–Wash group at the University of Washington responded by developing a torsion balance mounted on a uniformly rotating platform. This technique provided smoothly-modulated signals for interactions with λ smaller than the Earth's radius, as well as for astronomical attractors, and, because the signal frequency could be made much higher than in the solar experiments, greatly reduced the uncertainties from noise and those systematic effects that rise sharply at low frequencies. The first result from this instrument [23], which appeared in 1987, ruled out the original fifth force proposal. However, the suggestion of a finite-ranged Yukawa interaction led physicists to broaden their view of EP tests to a search for Yukawa interactions at all all accessible length scales.

The Eöt–Wash measurements with rotating platforms were subsequently refined [11,12] by improving the experimental precision and by expanding the number of test-body pairs and attractors to address specific issues. However, these and other [9,24–26] experiments were relatively insensitive for ranges $0.01\ \mathrm{m} < \lambda < 1\ \mathrm{m}$. To better constrain the strength of an interaction with this range, as well as to study an attractor with an N/Z ratio much different from the Earth, a stationary torsion balance and a rotating 3-ton attractor of depleted uranium were constructed [10].

2.3.3. *Tests of the strong equivalence principle*

The best current test of the Strong EP – the prediction that gravitational binding energy falls like any other form of mass and energy – comes from lunar laser ranging (LLR) [27]. This test probes the non-linear nature of general relativity, how gravity itself begets gravity, by comparing the gravitational accelerations of the Earth and Moon toward the Sun. The Earth and Moon form an important test-body pair because gravitational binding energy gives a -4.6×10^{-10} contribution to the Earth's mass but only -0.2×10^{-10} to the Moon's. If the Strong EP were violated, these accelerations would not be precisely equal, causing the Moon's orbit around the Earth to be polarized in a characteristic way that would show up as a periodic deformation of the laser range. Three and a half decades of LLR data, coupled with sophisticated modeling, reveal that the Earth-Moon differential acceleration toward the Sun is $\Delta a_{LLR}/g_{\odot} = (-1.0 \pm 1.4)^{-13}$, which corresponds to $\eta_{SEP} \equiv (a_e - a_m)/(-4.45 \times 10^{-10} g_{\odot}) = (2.3 \pm 3.2) \times 10^{-4}$. However, as pointed out by Nordtvedt [28], this important and impressive test is ambiguous. The Earth and Moon test bodies differ not only in their fractions of gravitational self-energy, but also in their composition. The Moon's composition is similar to that of the Earth's mantle, but the Earth has a massive Fe-Ni core while the Moon does not. Hence the LLR test simultaneously probes both the Weak and the Strong EP, so that it is possible that the two contributions tend to cancel. Nordtvedt noted that there exists a class of metric theories of gravity that respect the Weak EP, but not the Strong EP and argued that the ambiguity in this fundamental test could be removed by a laboratory experiment that compared the accelerations toward the sun, Δa_{CD}, of test bodies having the compositions of the Earth and Moon; a composition dependent acceleration (Weak EP violation) would be identical for the laboratory and LLR cases, so that subtracting the lab differential acceleration from Δa_{LLR} would give a rigorous test of the Strong EP. Baeßler et al. [8] implemented Nordtvedt's general idea but made a change that enhanced the experimental sensitivity. They fabricated two Earth core (EC) and two Moon–Earth mantle (MM) test bodies and studied their differential acceleration toward the Sun. The Earth-core test bodies were made from an iron, nickel and chromium alloy. The Moon–Earth mantle test bodies were made from quartz and a magnesium alloy. Both kinds of test bodies had the same outer dimensions and were gold coated on all outer surfaces. An improved version of the Baeßler et al. measurement [29] found a composition-dependent acceleration of $\Delta a_{CD}/g_{\odot} = (+1.0 \pm 1.4) \times 10^{-13}$. This gives a loop-hole free value for the Strong EP test of $\Delta a_{SEP}/g_{\odot} \equiv (\Delta a_{LLR} - \Delta a_{CD}) = (-2.0 \pm 2.0) \times 10^{-13}$, which implies

$$\eta_{SEP} = (+4.4 \pm 4.5) \times 10^{-4}. \tag{15}$$

2.3.4. *A recent experiment*

A new EP test, recently reported by the Eöt–Wash group [12], illustrates the state of the art. Fig. 3 shows a cross sectional drawing of the apparatus. The vacuum chamber containing the torsion pendulum is suspended from an air-bearing turntable, which rotates at a constant rate with a period of about 20 min. The rotation axis is kept within a few nanoradians of local vertical by a tilt-control system. The pendulum twist is continuously monitored by a co-rotating autocollimator that shines a collimated laser beam onto the pendulum. Four mirrors on the pendulum allow measurements at four different pendulum orientations so that the EP signal can be separated from small non-uniformities in the turntable rotation rate, which are unchanged under rotation of the pendulum.

The pendulum is suspended from a 1.0 m long and 20 μm thick tungsten fiber that provides a restoring torque of $\kappa = 2.34 \times 10^{-9}$ N m/rad and a $Q \approx 5000$. The pendulum is shown in Fig. 3. It has a four-fold azimuthal and up–down reflection symmetries. Because of the high degree of symmetry, the inner mass moments with $1 \leq l \leq 5$, $m \leq 2$ are very small, and the gravitational coupling to the environment is reduced. The pendulum carries eight barrel-shaped test bodies, four made from Be and four either from Ti or Al. The denser test bodies are hollow so that they have the same mass as the Be bodies. Together, the test bodies comprise more than half the pendulum's total mass. The test bodies can be exchanged to invert the composition dipole with respect to the pendulum frame, a procedure that helps to investigate and then suppress systematic effects associated with the pendulum frame and its suspension system.

The location of the apparatus, nearly half way up an exterior wall in a partially underground room, was chosen to maximize the Yukawa signal for $\lambda > 1$ m. A substantial effort was made to measure, minimize and then estimate uncertainties from residual gravitational couplings. The balance is surrounded with 800 kg of lead designed to compensate the local Q_{21} and Q_{31} gradients. The compensators are mounted on a turntable that can be rotated around the pendulum to double the ambient gravity gradients. This feature was used to infer the pendulum's residual q_{21} moment, which was then

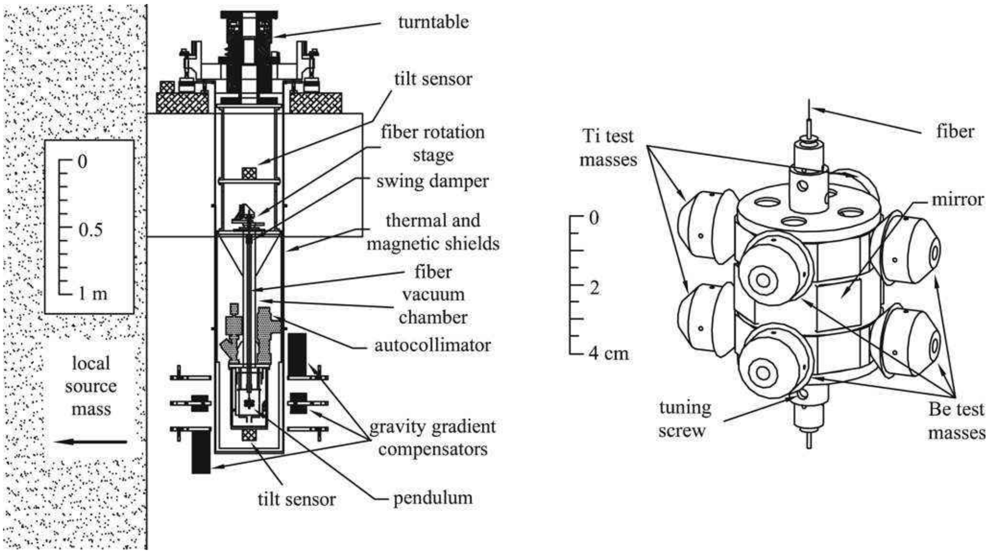

Fig. 3. Cross section of the apparatus on the left and a three dimensional drawing of the pendulum on the right.

further reduced by adjusting small tuning screws on the pendulum, shown in Fig. 3. The outer mass moments Q_{21} and Q_{31} were monitored by replacing the EP pendulum with a specially designed gravitometer pendulum that was configured to be highly sensitive to either the Q_{21} or Q_{31} moments.

The turntable consists of a high-quality aluminum air-bearing, to which an optical angle encoder is attached. The turntable rotation rate is controlled by a digital feedback loop that generates a rotating magnetic field that applies torques on a coaxial copper cylinder mounted directly on the turntable rotor. The optimal signal-to-noise ratio of the torsion balance occurred at a rotation rate of about 1 mHz. Non-linearities in the angle encoder were mapped out by operating the turntable at rotation rates well above the free resonance frequency of the pendulum. In this situation, the pendulum cannot respond to any torque, and an apparent twist must be due to a variation in the turntable's rotation rate. The turntable is operated at precisely 2/3 of the pendulum's resonant frequency to ensure that data segments contain an integer number of rotation and torsion pendulum cycles.

75 days and 96 days of data were acquired with Be–Ti and Be–Al composition dipoles, respectively. The physical locations of the test bodies on the pendulum were interchanged once for each test-body pair. The resulting differential accelerations for two sets of test body pairs in the field of the Earth are

$$\begin{aligned}
&a_N(\mathrm{Be}) - a_N(\mathrm{Ti}) = (+0.6 \pm 3.1) \times 10^{-15}\ \mathrm{m/s^2} \Rightarrow \eta_\oplus(\mathrm{Be,Ti}) = (+0.3 \pm 1.8) \times 10^{-13}\\
&a_W(\mathrm{Be}) - a_W(\mathrm{Ti}) = (-2.5 \pm 3.5) \times 10^{-15}\ \mathrm{m/s^2}\\
&a_N(\mathrm{Be}) - a_N(\mathrm{Al}) = (-2.6 \pm 2.5) \times 10^{-15}\ \mathrm{m/s^2} \Rightarrow \eta_\oplus(\mathrm{Be,Al}) = (-1.5 \pm 1.5) \times 10^{-13}\\
&a_W(\mathrm{Be}) - a_W(\mathrm{Al}) = (+0.7 \pm 2.5) \times 10^{-15}\ \mathrm{m/s^2}.
\end{aligned} \tag{16}$$

The subscripts N and W denote accelerations toward the North and West. All these results support the EP and $\eta_\oplus$ has been determined a factor 10 more precisely than in a previous experiment [11].

These differential accelerations can been converted into limits on $\tilde{\alpha}$ by integrating the charge to mass ratio and Yukawa factor over the attractor volume for each value of λ. For $\lambda < 10$ km, topographical maps of the Seattle environment were used to infer the mass and charge distributions of the environment. The different "charges" of water and soil were taken into account. An elliptical layered Earth model [11,30,31] was used for ranges $\lambda > 1000$ km. Preliminary calculations indicate that the attractor strength in the intermediate region is at least equal to that for $\lambda = 10$ km.

In addition to the differential accelerations toward laboratory-fixed attractors, differential accelerations toward astronomical attractors were determined by fitting the data to the modulated accelerations caused by the astronomical object as shown in Fig. 4. Preliminary values for differential accelerations toward the Sun and the center of our galaxy are

$$\begin{aligned}
&a_\odot(\mathrm{Be}) - a_\odot(\mathrm{Ti}) = (-1.8 \pm 2.8) \times 10^{-15}\ \mathrm{m/s^2} \Rightarrow \eta_\odot(\mathrm{Be,Ti}) = (-3.1 \pm 4.7) \times 10^{-13}\\
&a_\odot(\mathrm{Be}) - a_\odot(\mathrm{Al}) = (0.0 \pm 2.5) \times 10^{-15}\ \mathrm{m/s^2} \Rightarrow \eta_\odot(\mathrm{Be,Al}) = (0.0 \pm 4.2) \times 10^{-13}\\
&a_g(\mathrm{Be}) - a_g(\mathrm{Ti}) = (-2.1 \pm 3.1) \times 10^{-15}\ \mathrm{m/s^2} \Rightarrow \eta_{DM}(\mathrm{Be,Ti}) = (-4.4 \pm 6.5) \times 10^{-5}\\
&a_g(\mathrm{Be}) - a_g(\mathrm{Al}) = (+1.6 \pm 2.8) \times 10^{-15}\ \mathrm{m/s^2} \Rightarrow \eta_{DM}(\mathrm{Be,Al}) = (+3.4 \pm 5.8) \times 10^{-5}.
\end{aligned} \tag{17}$$

No significant deviations from the EP were observed for any attractor and the value for η_{DM} has been improved, compared to Ref. [11], by a factor ≈10.

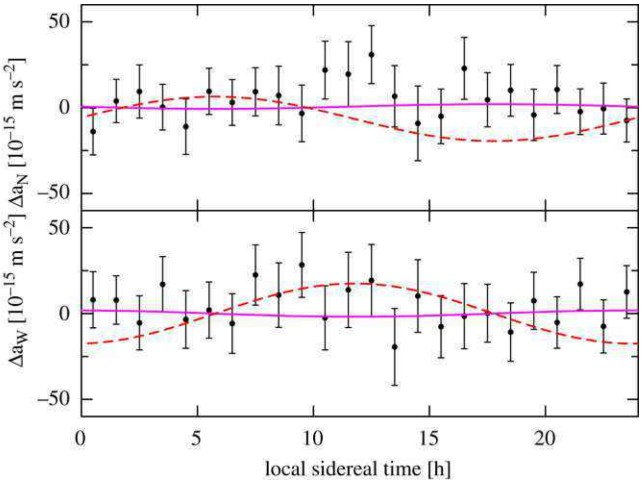

Fig. 4. The average differential acceleration of Be and Ti decomposed in the north and west component and grouped into bins of sidereal hours. The solid line is a fit for an acceleration towards the galactic center and its quadrature component. The dashed line shows a hypothetical signal of 20×10^{-15} m/s^2 towards the center of the galaxy.

2.4. Implications for new forces

The resulting limits on long-ranged interactions coupling to Z, N and B are shown in three exclusion plots in Fig. 5. For ranges $\lambda > 10^7$ m forces almost 11 orders of magnitude weaker than gravity are ruled out with 95% confidence. This result is impressive, considering that gravity is about 38 orders of magnitude weaker than the electro-magnetic interaction.

Fig. 5 also shows how the limits on $\tilde{\alpha}$ of an infinite-range Yukawa interaction depend on the charge parameter $\tilde{\psi}$. The shaded area is excluded by the results from Refs. [20,32] with 95% confidence. Each limit has two pronounced maxima. The poles at $\psi \approx 45°$ are caused by the vanishing charge differences of the test bodies. Poles at negative angles arise from the vanishing charge of any single attractor. Braginsky and Panov [20] used the Sun as their only attractor, and so have an attractor pole. The Eöt–Wash result is based on attraction to the Earth as well as to the Sun so that the pole at negative angles disappears.

2.5. Future prospects

Searches for new interactions can be made more sensitive over a wide range of $\tilde{\psi}$ by using a hydrogen-rich material, such as ultra-high molecular weight polyethylene (PE), for one member of the test-body pair. In order to match PE's low density, it is best paired with Be. This combination has a 50% higher $\Delta[\tilde{q}/\mu]$ than the Al and Pt pair employed by Braginsky.

APOLLO, a next-generation LLR facility at the Apache Point Observatory, has recently demonstrated ranging uncertainties of 1 mm [35]. This represents an order of magnitude improvement over previous work, and should lead to a 10 times more precise value for the EP-violating differential acceleration of the Earth and Moon toward the Sun. To keep pace with these advances, it is important to make a better torsion-balance measurement with Earth-core-like and Moon-like test bodies. The Eöt–Wash group have currently installed a pendulum with EC and MM test bodies in the instrument described in Section 2.3.4. They hope to achieve a differential acceleration sensitivity that is 10 times better than Ref. [29] and tighten the Strong EP test.

An order of magnitude improvement over the current limits on $\tilde{\alpha}$ may be possible with cryogenic torsion balances. At liquid helium temperatures the $\sqrt{k_B T}$ is reduced by a factor 9; furthermore, the quality factor Q of metal fibers can be as high as 100,000, compared to ≈5,000 at room temperature [36]. This suggests that the statistical uncertainty, which is currently the largest contribution to the total uncertainty, can be reduced by a factor of 40.

A significant sensitivity improvement may come from "free-fall" satellite and balloon instruments. To our mind, the main advantage of such measurements over torsion-balance experiments is that the "free fall" experiments see the entire differential acceleration, while torsion balance experiments see only its horizontal component, which is only $\sim 10^{-3}$ of the effect. While the satellite experiments have proposed sensitivities many orders of magnitude better than current ground-based experiments it should be noted that they are only sensitive to interaction ranges larger than the altitude of the orbit.

Reasenberg [37] has proposed a sounding-rocket experiment, where the trajectories of two test body pairs in free fall will be compared. The proposed sensitivity is $\eta \leq 10^{-16}$ for a single flight. Several satellite experiments have been proposed and some are funded [38–42]. A cryogenic STEP (Satellite Test of the Equivalence Principle) experiment was proposed in 1976 by Worden [38,39] that would use SQUIDs to determine the relative acceleration of two masses in a concentric arrangement. It is currently believed that STEP could achieve a sensitivity of $\eta \approx 10^{-18}$. MICROSCOPE (Micro-Satellite à traînée Compensée pour l'Observation du Principle d'Equivalence), proposed by the French Aerospace Laboratory ONERA, has a projected launch

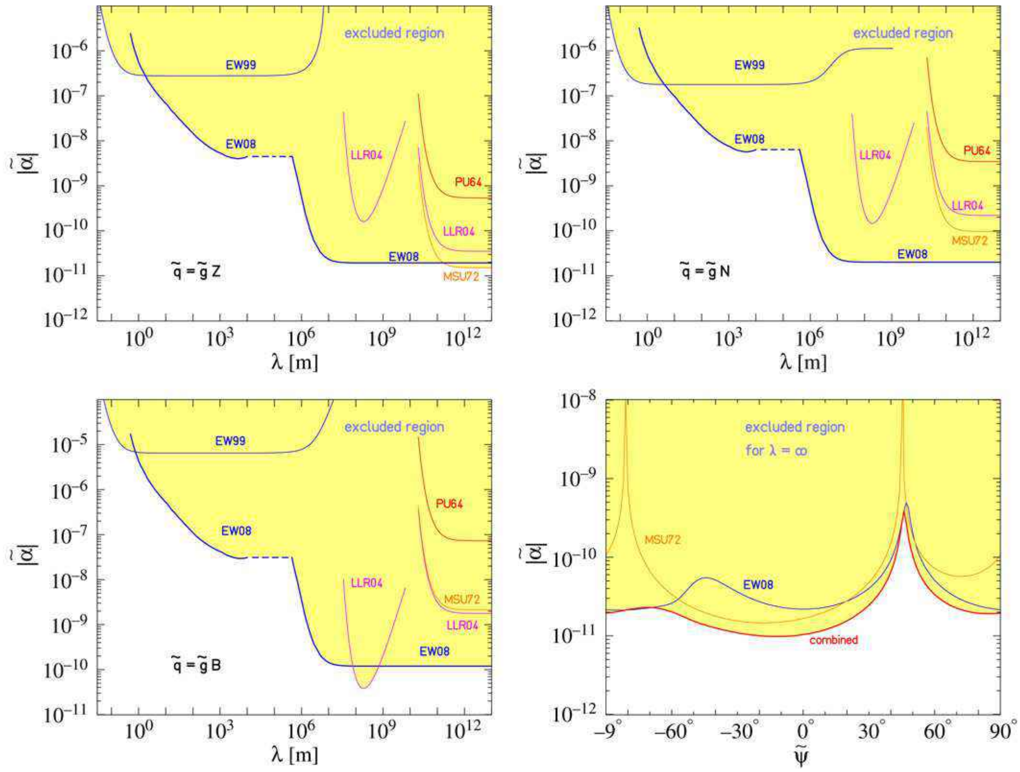

Fig. 5. Limits on EP-violating Yukawa interactions. The upper left and right panels show coupling to Z and to $N = B - L$, respectively; the lower left panel shows the coupling to B. The lower right panel displays the limits on the strength of a $\lambda = \infty$ Yukawa interaction as a function of the charge parameter $\tilde{\psi}$. All shaded regions are exluded with 95% confidence. The labels link to the references as follows: PU64 — [19], MSU72 — [20], EW99 — [10], LLR04 — [27, 33,34], EW08 — [32].

date of 2010 and a proposed sensitiviy of $\eta \approx < 10^{-15}$ [40]. The satellite will carry two differential accelerometers that compare the forces on two coaxial cylinders, using an electrostatic feedback mechanism. The outer cylinder of the science accelerometer will be made from Ti, the inner from a Pt/Rh alloy. Both cylinders of the "base-line" accelerometer will be built from the Pt/Rh alloy. The satellite will be injected into a heliosychronous orbit at 800 km altitude. The Italian Space Agency (ASI) is considering a proposal by Nobili [41] to launch a satellite dubbed GG (Galileo Galilei) that contains two cylindrical test bodies in a concentric geometry. In contrast to MICROSCOPE, it is planned to spin the spacecraft at a high frequency of $\approx$2 Hz to improve the signal to noise ratio. GG is projected to resolve η to $\approx 10^{-17}$.

3. Short-range tests of the gravitational inverse-square law

3.1. Parameterizations

Experimental limits on violation of the gravitational inverse-square law (ISL) are usually expressed as constraints on an additional Yukawa interaction that gives a modified gravitational interaction between point bodies with masses m_1 and m_2 of the form

$$V(r) = -G_N \frac{m_1 m_2}{r}\left(1 + \alpha \mathrm{e}^{-r/\lambda}\right). \tag{18}$$

This, of course, is the static potential produced by the exchange of natural-parity (0^+, 1^-, 2^+, etc.) bosons between unpolarized bodies, where the boson mass is $\hbar c/\lambda$. It also is expected to approximate well the effect of "large extra" dimensions, as long as r is greater than the largest size of the extra dimensions [2]. Note that α must be distinguished from the $\tilde{\alpha}$ (defined in Eq. (5)) that characterizes experimental constraints on EP violation; $\tilde{\alpha}$ multiplies not the mass but rather the "charge"-to-mass ratio, $\tilde{q}/\mu$, of the interacting bodies. Because the fractional difference in $\tilde{q}/\mu$ values of EP test bodies is typically quite small, ISL tests are in some ways more sensitive than EP tests. On the other hand, ISL tests are completely insensitive to new interactions mediated by massless bosons. Note that, in contradistinction to EP experiments, any given ISL test, which can be thought of as comparing the forces at two different length scales r_1 and $r_2 > r_1$, is sensitive only to violations with $r_1 \lesssim \lambda \lesssim r_2$. On the other hand, EP experiments, which compare the accelerations of two different materials, can be sensitive to Yukawa EP violation with $r \lesssim \lambda \lesssim \infty$, where r is distance from the detector to the attractor.

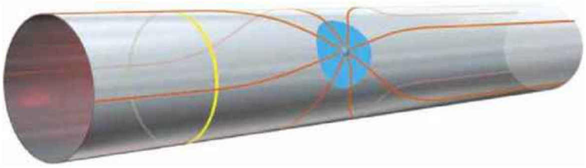

Fig. 6. Cartoon illustrating the effect of a curled-up large extra dimension on the gravitational force. The cartoon shows one ordinary dimension and one curled up extra dimension. All non-gravitational physics is assumed to be confined to the ordinary dimension, and only gravity can expand into the extra dimension. The gravitational lines of force from a point mass placed on our *x*-axis (which runs from left to right) are shown. As we probe the gravitational force, by moving away from the point mass along the *x* axis, we find that for separations small compared to the radius *R* of the curled-up dimension, the lines of force diverge, *i.e.* a $1/r$ force (Gauss's Law in 2 dimensions). But as we move along the x axis farther from the point mass the lines cannot expand any further and become parallel, *i.e.* a constant force (Gauss's Law in 1 dimension.) The transition from constant to $1/r$ force laws is smooth, and is well approximated by an additional Yukawa term as long as $r > R$ (see citations in Ref. [2]). Figure courtesy of Savas Dimopoulos.

In some contexts, instead of Yukawa ISL violation, one may find power-law potentials, which can be written in the form

$$V_{ab}^{k}(r) = -G\frac{M_aM_b}{r}\beta_k\left(\frac{1\text{ mm}}{r}\right)^{k-1}. \tag{19}$$

Such power-law interactions can be produced by higher-order exchange processes with simultaneous exchange of multiple massless bosons. These second-order processes are particularly interesting when the exchanged particles are unnatural-parity (0^-, 1^+, etc.) bosons (for which the 1st-order force vanishes when averaged over unpolarized test bodies) or else fermions (for which the 1st-order process is forbidden). For this reason, experimental constraints on couplings of unnatural-parity bosons are typically quite poor, and the most stringent bounds often come from astrophysical considerations [43]. Potentials with $k = 2$ are generated by the simultaneous exchange of two massless scalar [44] bosons. Simultaneous exchange of massless pseudoscalar [45] particles between fermions a and b with γ_5-couplings to g_a and g_b, gives a $k = 3$ potential

$$V_{ab}(r) = -\frac{\hbar}{c^3}\frac{1}{64\pi^3}\frac{(g_P^a g_P^b)^2}{M_aM_b}\frac{1}{r^3}. \tag{20}$$

Potentials with $k = 5$ are produced by the simultaneous exchange of two massless pseudoscalars with $\gamma_5\gamma_\mu\partial^\mu$ couplings such as axions or Goldstone bosons [45], or from massless ν-$\bar{\nu}$ pairs [46]. Power-law potentials with fractional k are expected from unparticle exchange [47].

If an ISL violation were observed, it would then be necessary to find if its form is described by Eq. (18) or (19), or perhaps by something more complicated, and to determine whether or not the new interaction violates the EP.

3.2. Motivation

Until a few years ago, it was widely assumed that the gravitational ISL should be valid for length scales from infinity to roughly the Planck length $R_P = \sqrt{G\hbar/c^3} = 1.6 \times 10^{-35}$ m, at which scale quantum effects must become important. After all, the usual argument went, the exponent 2 in the force law simply reflects the fact that we live in a 3-dimensional world. A wide variety of recent theoretical speculations, motivated in large part by string-theory considerations, have raised the possibility that fundamentally new phenomena could occur in the largely unexplored regime of length scales between 10 microns and 1 mm. Two inherent features of string theory undergird these speculations: the theory inherently contains extra dimensions and predicts large numbers of extra particles, both of which may appear as violations of the inverse square law. An extensive review [2] of these speculations has recently appeared, and we refer the reader to this paper for a considerably more complete discussion of the topic.

Many of these ideas are driven by the two so-called hierarchy problems of gravity:

- *The gauge hierarchy problem.* Gravity is extraordinarily weak compared to the other fundamental forces. The Planck mass $M_P = \sqrt{\hbar c/G} = 1.2 \times 10^{16}$ TeV/c^2 is huge compared to the electroweak scale $M_{EW} \sim 1$ TeV/c^2. It has been argued [48] that that the true Planck mass, M_*, could be in the TeV/c^2 range if some of the "extra" space dimensions demanded by string-theory are curled up with a radius large compared to the Planck length. It is possible that the size of some of the "large extra dimensions" could be large enough to alter the gravitational Gauss Law from $1/r^2$ to $1/r^{2+n}$ (n is the number of large extra dimensions) at small separations r. Fig. 6 schematically illustrates the effect. The additional volume provided by the extra dimension(s), assumed to be accessible only to the gravitational interaction, would normally allow most of the real strength of gravity to disappear into the extra dimension(s), but would have the effect of making gravity become anomalously strong for sufficiently small separations, indicating that the "true" Planck mass could be as small as a few TeV [48]. Others [49] have suggested that an extra time dimension would cause a weakening of gravity at small separations.
- *The cosmological constant problem.* The observed gravitating vacuum-energy density is vanishingly small, compared with the predictions of quantum mechanics. The gravitating energy density $\rho_{\text{vac}} \sim 0.7\rho_c$, inferred from a wide variety of astrophysical observations [1,50,51], is at least 10^{60} times smaller (if supersymmetry is "just around the corner") and

possibly 10^{120} times smaller (if supersymmetry is not valid) than the predicted zero-point energy for a cutoff of M_P. The observed energy density corresponds to a length scale $R_{\rm vac} = \sqrt[4]{\hbar c/\rho_{\rm vac}} \approx 85~\mu$m and an energy of $\sqrt[4]{(\hbar c)^3\rho_{\rm vac}} \approx 2$ meV that may have fundamental significance [52]. It has been suggested that the apparent inability of gravity to "see" the vacuum energy could be explained if the effective theory of gravity had a cutoff of ∼1 meV [53], so that gravity would effectively "shut off" at length scales less than $R_{\rm vac}$.

Experimental tests of the gravitational ISL also probe speculations about "non-gravitational" particle physics. It is widely believed that the Standard Model of particle physics cannot be complete. Many ideas for extending the Standard Model predict very-low-mass scalar or vector bosons that would produce short-range exchange forces which could appear as violations of the ISL. Ref. [2] provides a recent, comprehensive review of these theoretical motivations. Since the publication of Ref. [2], two new theoretical proposals with particular relevance to ISL tests have appeared.

- String theories generically predict scalar particles (the dilaton and large numbers of moduli) that are initially massless. Essentially massless scalar fields are also frequently invoked by cosmologists. However, the exchange forces these bosons mediate would produce apparent violations of the equivalence principle that are not consistent with the extremely tight constraints from laboratory tests discussed above. The "chameleon mechanism" was recently invented [54] to "hide" such bosons from the classic experimental constraints derived from centimeter to astronomically-sized test bodies. Chameleon exchange leads to an effective potential density [55]

$$V_{\rm eff}(\phi,\vec{x}) = \frac{1}{2}m_\phi^2\phi^2 + \frac{\gamma}{4!}\phi^4 - \frac{\beta}{M_{\rm Pl}}\rho(\vec{x})\phi, \tag{21}$$

  where ϕ is the scalar field, γ characterizes the strength of its self interaction, β characterizes its coupling to matter, and $M_{\rm Pl}$ is the reduced Planck mass. The "natural" values of β and γ are ≈1. In the presence of matter with density ρ, a massless chameleon field acquires an effective mass [55],

$$m_{\rm eff}(\rho) = \frac{\hbar}{c}\left(\frac{9}{2}\right)^{1/6}\gamma^{1/6}\left(\frac{\beta\rho}{M_{\rm Pl}}\right)^{1/3}, \tag{22}$$

  that dramatically weakens experimental constraints, because only a small amount of material near the surface with thickness $\mathcal{O}(\hbar/(m_{\rm eff}c))$ contributes to a long-range force [54–57]. For $\rho = 10$ g/cm^2 and $\beta = \gamma = 1$, this skin thickness is about 60 μm.
- It has been suggested that 'unparticles" (non-trivial scale invariant manifestations of an effective field theory [58]) might exist, and that these could produce apparent violations of the ISL with the character of a power-law potential with fractional powers [47].

3.3. *Experimental issues*

3.3.1. *Geometries*

The most effective geometry for detecting short-range ISL violation is plane-on-plane. This allows one to place the most matter within a given minimum separation between attractor and detector, and makes it practical to place a rigid conducting membrane between the attractor and detector, which is essential if one is to study short-range gravity and not the electrical properties of surfaces. The potential energy from a Yukawa interaction between a flat detector plate of area A_d, thickness t_d and density ρ_d a distance s from an infinite attractor plate of thicknesses t_a, and density ρ_a, is

$$V_Y = 2\pi\alpha G\rho_d\rho_a\lambda^3A_d[1-{\rm e}^{-t_d/\lambda}][1-{\rm e}^{-t_a/\lambda}]{\rm e}^{-s/\lambda}. \tag{23}$$

Torsion balance experiments have used two different methods to probe this interaction. The most straightforward method is simply to measure the variation of the force of attraction on a plane detector

$$F_Y = 2\pi\alpha G\rho_d\rho_a\lambda^2A_d[1-{\rm e}^{-t_d/\lambda}][1-{\rm e}^{-t_a/\lambda}]{\rm e}^{-s/\lambda}, \tag{24}$$

as the distance, s, to its effectively infinite plane attractor is modulated at frequency ω. In this case, for λ much less than the plate thicknesses, the ratio of Yukawa to Newtonian forces becomes

$$\frac{F_Y(s)}{F_N} \approx \alpha\frac{\lambda^2}{t_dt_a}{\rm e}^{-s/\lambda}, \tag{25}$$

which is a true null design as F_N is independent of s. This method, used in Ref. [59] has the advantage that its inherent sensitivity scales as $\lambda^2{\rm e}^{-s/\lambda}[1-{\rm e}^{-t_d/\lambda}][1-{\rm e}^{-t_a/\lambda}]$, but the disadvantage that the signal frequency is identical to the disturbance frequency ω.

An alternative method that provides a large separation between signal and disturbance frequencies was employed in Refs. [60–62]. This method measures the torque on a circular detector produced by a circular attractor that rotates underneath the detector at a frequency ω, as shown in Fig. 7. The detector and attractor are cylindrically symmetrical, except that both have a series of round holes equally spaced around their azimuths. In effect one is studying the interaction

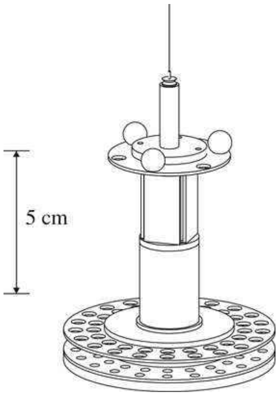

Fig. 7. Scale drawing of the detector and attractor used in Ref. [62]. The 42-hole tungsten attractor and detector disks have thicknesses of 1 mm and have 21-fold rotational symmetry. The attractor contains a second, thicker disk, mounted below the upper attractor disk. The holes in the lower attractor are displaced by $\pi/21$ rad from the holes in the upper attractor, and are designed to cancel the 21ω Newtonian torque on the detector produced by the upper set of attractor holes. However, the lower disk cannot cancel a short-range interaction, because it is too far from the attractor. The 3 small spheres near the top of the detector were used for a continuous gravitational calibration of the torque scale. The four rectangular plane mirrors below the spheres were part of the twist-monitoring system. The detector's electrical shield is not shown. This experiment determined the gravitational torque by measuring the pendulum's twist as discussed in Section 6. Data were taken at attractor-to-detector separations between 9.5 mm and 55 μm.

between the "missing masses" in the detector and attractor holes. In this case, for N attractor and detector holes, each with area A_h, and for λ small compared to the dimensions of the holes, the Yukawa torque is

$$T \approx 2\pi\alpha G R \rho_d \rho_a \lambda^3 \frac{\partial A}{\partial\theta}[1-\mathrm{e}^{-t_d/\lambda}][1-\mathrm{e}^{-t_a/\lambda}]\mathrm{e}^{-s/\lambda}, \tag{26}$$

where R is the distance of the hole centers from the symmetry axes of the attractor and detector, θ is the angular orientation of the attractor, and A is the "overlap area" between the attractor and detector holes. N times per attractor revolution, A varies from $A = NA_h$ to $A = 0$ so that $\partial A/\partial\theta \approx NA_h/\pi$, producing signals at frequencies $N\omega$, $2N\omega$, $3N\omega$, etc. This technique has the disadvantage that its ultimate sensitivity scales as $\lambda^3\mathrm{e}^{-s/\lambda}[1-\mathrm{e}^{-t_d/\lambda}][1-\mathrm{e}^{-t_a/\lambda}]$ and it is not a null experiment. However, as implemented in Refs. [60,62], the missing mass technique was a "nearly null" experiment. The Newtonian $N\omega$ signal was canceled by making a two-layer attractor as shown in Fig. 7. The cancelation can only be exact for one particular detector-to-attractor separation, but is substantial at all detector-attractor separations, and greatly reduces the Newtonian signal, which diminishes the sensitivity of the experiment to scale factor uncertainties.

3.3.2. Backgrounds

Neglecting edge effects, the attractive electric force between a conducting plate with area A_d parallel with an infinite conducting plate is

$$F_E(s) = \epsilon_0 A_d V^2/(2s^2), \tag{27}$$

where V is the potential difference between the plates and ϵ_0 is the permittivity of free space. For 0.1 mm thick plates with densities of 10 g/cm^3, separated by 0.1 mm, F_E becomes as large as F_N for a potential difference of 1 mV; furthermore, the electric force grows with decreasing separation while the Newtonian force is constant.

The Casimir force between two grounded, perfectly conducting, smooth, infinite planes at zero temperature, separated by a distance s, is attractive

$$\frac{F_C}{A} = \frac{\pi^2\hbar c}{240 s^4}. \tag{28}$$

For a 0.1 mm thick plate of area A_d near an infinite plate of thickness 0.1 mm (again, both with density 10 g/cm^3), F_C becomes equal to F_N at a separation of $d = 40$ microns.

Systematic effects from these electrical forces can be eliminated by surrounding the detector with a *rigid* conducting shield. However, the conventional electrostatic force gives a significant contribution to the noise. Even if the detector and its shield are at the same average potential, they experience a residual electric interaction from patch fields–spatially varying microscopic electric potentials found on the surface of materials [63]—that arise because different crystal planes of a given material have, in general, different work functions [64]. To the extent that the surface is a mosaic of random microscopic crystal planes, there will be local potential differences with a scale size comparable to the size of the microcrystals. For example, different planes of W crystals have work functions that vary by 0.75 V. Gold is a good choice for test-body coating, as the work functions of its crystal planes vary by only 0.16 V. Surface contaminants also contribute to the local variation of the electric potential, altering the local work function and providing sites for the trapping of electrical charge. In the limit that

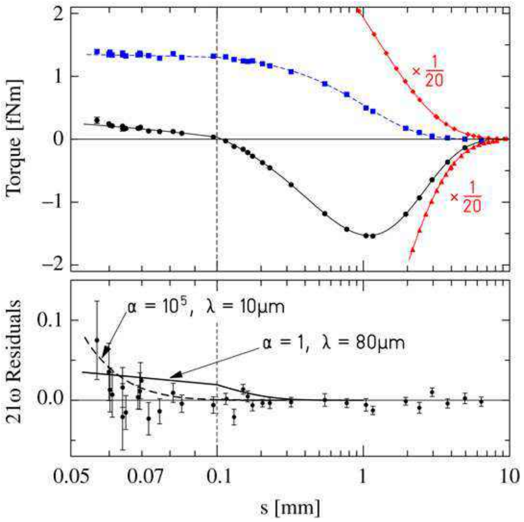

Fig. 8. Observed torques as a function of attractor-to-detector separation, s, from one of three data sets in Ref. [62]. The horizontal scale is expanded below $s = 100\ \mu\text{m}$. The upper panel displays the 21ω and 42ω torques as solid circles and squares, respectively. Diamonds (triangles) show the 21ω torque from the upper (lower) attractor plate alone; these illustrate the degree of cancelation of Newtonian gravity, which is exact at $s \approx 100\ \mu\text{m}$. When not visible the errors are smaller than the size of the points. The smooth curves show the Newtonian fit to the combined data of all 3 data sets. The lower panel shows the 21ω residuals; the solid and dashed curves show the residuals expected from $\alpha = 1$, $\lambda = 80\ \mu\text{m}$ and $\alpha = 10^5$, $\lambda = 10\ \mu\text{m}$ Yukawa interactions, respectively. Both are excluded by these results.

Table 5
68% confidence laboratory constraints on power-law potentials of the form given in Eq. (19)

k	$\lvert\beta_k\rvert$ [75]	$\lvert\beta_k\rvert$ (previous work [61,70])
2	4.5×10^{-4}	1.3×10^{-3} [70]
3	1.3×10^{-4}	2.8×10^{-3} [61]
4	4.9×10^{-5}	2.9×10^{-3} [61]
5	1.5×10^{-5}	2.3×10^{-3} [61]

the patches are smaller than the separation, the patch field force [63] scales as $1/d^2$. These patch fields are not only spatially inhomogeneous (which contributes to torque noise because the pendulum inevitably has some swing-mode motion), but also appear to be time dependent. Excess noise from time-dependent patch fields has been observed in miniature ion traps used to study cavity QED [65,66]. This excess torque noise at small detector-to-shield separations, which seemed to have a white power spectrum, was a limiting factor for the shortest-range constraints obtained in Ref. [62].

3.4. Results and implications

Our main focus is on gravitational strength phenomena. Although Casimir-force [67] and ultra-cold neutron [68] experiments probe very short length scales, they are sensitive only to forces vastly stronger than gravity, and therefore are beyond the scope of this paper. The current constraints on Yukawa violations of the ISL for λ between 1 μm and 1 cm are shown Fig. 9. The tightest constraints for λ between $\sim$ 10 μm and $\sim$4 mm come from Ref. [62]. Some of the data from that experiment are shown in Fig. 8. Constraints for λ between 1 cm and 10^{15} m, largely obtained from astronomical tests, are given in Fig. 10. The general trend for the constraints to become weaker as λ decreases is explained by the scaling laws mentioned above. Constraints for $\lambda \leq 1\ \mu\text{m}$, which are not tight enough to probe gravitational physics, can be found in Ref. [2]. The data in Fig. 9 show that any gravitational-strength ($|\alpha| = 1$) Yukawa interaction must have $\lambda \leq 56\ \mu\text{m}$.

The equivalent constraints on power law violations of the ISL are shown in Table 5.

3.4.1. Large extra dimensions

The results in Fig. 9 can be used to set a model-independent upper limit on the radius, R^*, of extra dimensions compactified on a torus. For minimum separations s_{min} greater than R^*, n such extra dimensions produce a signal that is well approximated by a single Yukawa interaction with $\alpha = 8n/3$ and $\lambda = R^*$ (see Ref. [2]). Therefore, the data of Ref. [62] set a 95%-confidence upper bound of $R \leq 44\ \mu\text{m}$ on the size of the largest extra dimension. For the two large extra-dimension scenario discussed in Ref. [48], the data require a 2σ lower limit on unification mass $M_* \geq 3.2\ \text{TeV}/\text{c}^2$, where M_* is defined in Ref. [61].

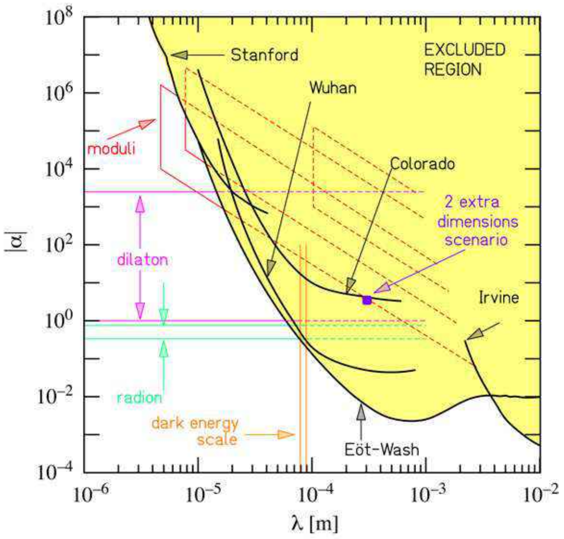

Fig. 9. Constraints on Yukawa violations of the gravitational $1/r^2$ law for $\lambda \leq 1$ cm. The shaded region is excluded at the 95% confidence level. Heavy lines labeled Eöt–Wash, Irvine, Wuhan, Colorado and Stanford show experimental constraints from Refs. [61,62,69,70,59,71–73], respectively. Lighter lines show various theoretical expectations summarized in Ref. [2].

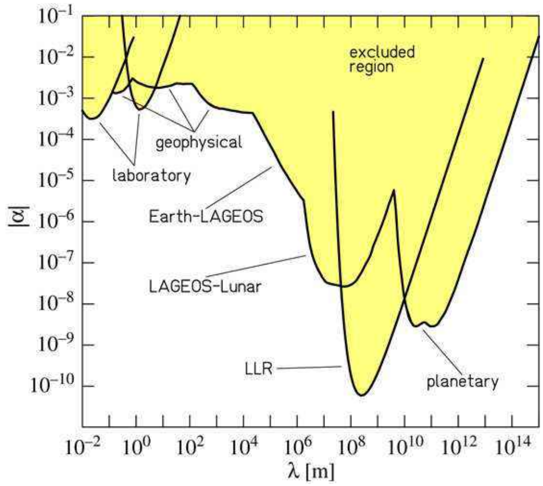

Fig. 10. Constraints on Yukawa violations of the gravitational $1/r^2$ law for $\lambda \geq 1$ cm. The shaded region is excluded at the 95% confidence level. Laboratory constraints are from Refs. [69,70,74]; geophysical and astronomical constraints are taken from an earlier review [2]. The LLR constraint is extracted from current published work [27] but is expected to improve in the future.

3.4.2. "Fat" gravitons

Sundrum [53] has conjectured that the cosmological constant problem, namely that the observed "dark energy" density has the same sign, but is much smaller than the vacuum energy density predicted by the usual rules of quantum mechanics, could be explained if the graviton were a "fat" object whose size ℓ_g prevents it from "seeing" the short-distance physics that dominates the vacuum energy. In his conjecture, the gravitational force vanishes at sufficiently small separations, compared with ℓ_g. Ref. [75] tested this scenario, by assuming that the gravitational force is

$$F_{12}^{\rm fat}(r) = -G\frac{M_1M_2}{r^2}\left[1-\exp(-.914r/\ell_g)^3\right], \tag{29}$$

which has a shape similar to the force shown pictorially in Fig. 8 of Ref. [53]; it vanishes at $r = 0$ and has a maximum at $r = \ell_g$. Sundrum argues that naturalness requires $\ell_g \geq 20$ μm. The results in Refs. [62,75], shown in Fig. 11, require $\ell_g \leq 98$ μm at 95% confidence. This upper limit on ℓ_g is larger than the 44 μm limit on the size of an extra dimension, because the data probe the large-distance tail of the new potentials, and the "fat-graviton" force falls off much more rapidly with increasing separation than does a Yukawa force.

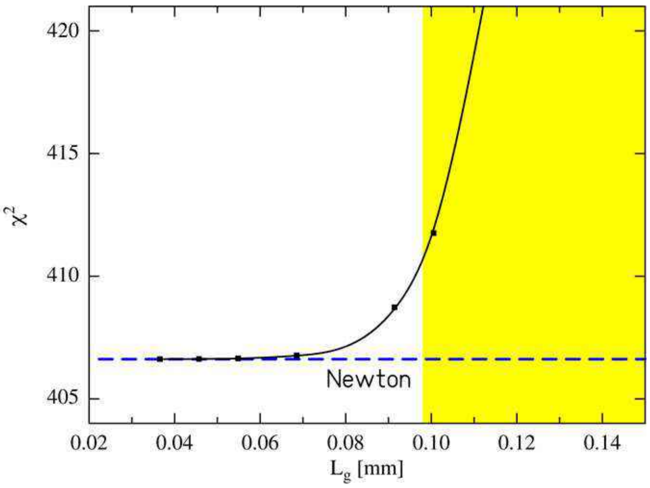

Fig. 11. Constraint on "fat graviton" interactions of the form given in Eq. (29) showing the χ^2 of the fit to the data of Ref. [75] as a function of ℓ_g. The shaded area is excluded with 95% confidence.

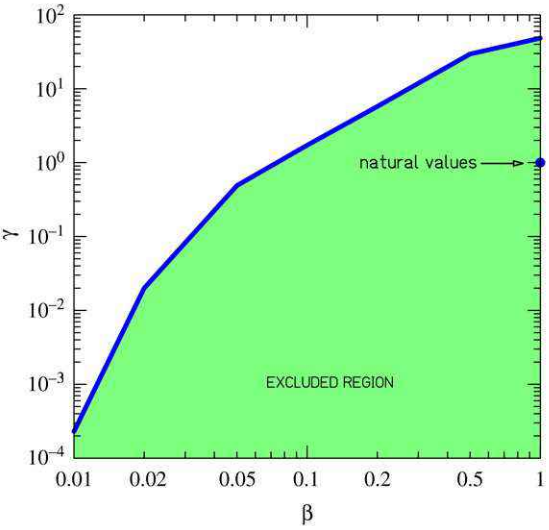

Fig. 12. 2σ constraints on the chameleon parameter β as a function of γ from the data of Ref. [62]. The shaded area is ruled out at 95% confidence. The chameleon signal is strongest when the chameleon length scale is comparable with the 1 mm hole thickness. For much larger length scales, the field varies little over the pendulum and attractor, giving a weak signal. For length scales much smaller than the 10 μm thickness of the electrostatic shield between the detector and attractor, the signal is "screened" by the shield.

3.4.3. Chameleons

Upadhye [75] has computed the constraints on chameleon self couplings and couplings to matter implied by the data of Ref. [62]. The results, shown in Fig. 12, handily exclude the natural values $\beta = 1$, $\gamma = 1$. In principle, the data provide constraints for $\beta > 1$, but the non-linear nature of the chameleons made quantitative calculations difficult in that regime.

3.4.4. Multiparticle and unparticle exchange forces

The limits on β_3 in Table 5, together with Eq. (20), provide the constraint on the γ_5 couplings of massless pseudoscalars to neutrons and protons,

$$\begin{aligned}\Gamma &\equiv \left[\frac{Z}{\mu}\right]^2 \frac{(g_P^p)^4}{(\hbar c)^2} + \left[\frac{N}{\mu}\right]^2 \frac{(g_P^n)^4}{(\hbar c)^2} + 2\left[\frac{Z}{\mu}\right]\left[\frac{N}{\mu}\right] \frac{(g_P^p)^2}{\hbar c}\frac{(g_P^n)^2}{\hbar c} \\ &= \beta_3 \frac{cG}{\hbar^3} 64\pi^3 u^4 (1\ \text{mm})^2 = 2.56 \times 10^{-10} \beta_3. \end{aligned} \tag{30}$$

(Couplings to electrons may be ignored [76] because of the very small upper limit on such couplings deduced from an electron-spin-dependence experiment.) The γ_5 couplings of massive pseudoscalars are also constrained by fitting the

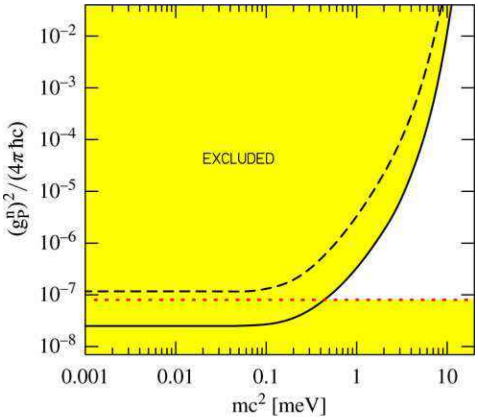

Fig. 13. (color online) 68%-confidence constraints on the γ_5 couplings of massive pseudoscalars to neutrons plotted against pseudoscalar mass m. The solid and dashed curves are from the ISL tests of Refs. [62,61] respectively. The horizontal dotted line shows the SN1987a constraint [43].

Ref. [62] data in terms of the Newtonian potential plus the appropriate generalization [77,78] of Eq. (20). The resulting bounds on g_P^n [75] are shown in Fig. 13. The observed SN1987a neutrino pulse excludes neutron couplings with $8 \times 10^{-14} < (g_P^n)^2/(4\pi\hbar c) < 8 \times 10^{-8}$ [43]. Stronger couplings are allowed because the pseudoscalars would have been trapped in the star. ISL results exclude this possibility for γ_5-coupled pseudoscalars with $mc^2 \leq 0.6$ meV. Helioseismology constraints on exotic energy loss processes provide a comparable bound on the coupling to protons, $(g_P^p)^2/(4\pi\hbar c) < 3 \times 10^{-9}$ [79].

3.5. *Future prospects*

It is difficult to predict the ISL constraints that will be forthcoming, because the results will almost surely be limited by systematic errors. We presume that several groups are working on short-range gravity experiments. The Eöt–Wash group has two such experiments in the commissioning stage, one is an evolution of the "missing mass" designs of Refs. [61,62]; the detector and attractor consist of 50 μm thick tungsten plates, each with 120 radial wedge-shaped holes with characteristic widths of ∼100 μm. The other is an "infinite plane" experiment.

4. Spin-pendulum experiments

4.1. *Motivation*

To minimize systematic errors associated with magnetic forces, the classic equivalence-principle and inverse-square-law torsion balance experiments used highly nonmagnetic, unpolarized test bodies. As such, these experiments were insensitive to interactions that might couple to intrinsic spin. A large body of theoretical work, on the other hand, predicts new spin-coupled interactions that may be observable with an electron-spin-polarized torsion pendulum. We divide the new spin-coupled interactions into three classes: preferred frame effects for which the spins in the pendulum couple to background fields that pervade space, spin interactions mediated by the exchange of unnatural parity (0^+, 1^-, etc.) bosons, and gravitational torsion.

4.1.1. *Preferred frames*

A preferred frame violates Lorentz invariance, and could cause the spins in the pendulum to have a preferred orientation in inertial space or a preferred helicity. The experimental signature for a violation of rotational invariance is a laboratory potential given by

$$V_A = -\boldsymbol{\sigma} \cdot \boldsymbol{A} \tag{31}$$

where $\boldsymbol{A}$ is the preferred direction in inertial space and $\boldsymbol{\sigma}$ is the electron spin.

A violation of boost invariance can generate a helicity dependent interaction

$$V_B = -B\boldsymbol{\sigma} \cdot \boldsymbol{v}/c, \tag{32}$$

where $\boldsymbol{v}$ is the velocity of the spin with respect to inertial space.

Kostelecký and others [80] also consider a tensor helicity-generating term that produces a laboratory interaction

$$V_C = -\sum_{i,j} \sigma_i \frac{v_j}{c} C_{ij}. \tag{33}$$

One might expect that such preferred-frame effects will be suppressed by the Planck scale, and therefore of order $m_e^2/M_{\text{Planck}} \approx 2 \times 10^{-17}$ eV. Spin-pendulum measurements are sufficiently sensitive to probe this energy scale.

The Standard Model Extension

The Standard Model Extension (SME), developed by Kostelecký and coworkers [80], gives rise to a preferred frame via fields that were spontaneously generated in the early universe and subsequently inflated to enormous sizes. Rotations and boosts of an observer remain Lorentz invariant, but these fields violate Lorentz invariance for particle transformations. The Lorentz non-invariance allows the construction of a field theory with both Lorentz and *CPT*-violating interactions. The SME has been widely used to quantify the sensitivity of various *CPT* and preferred-frame tests involving photons, leptons, mesons and baryons. Ref. [81] has an extensive set of references to this work.

The $\boldsymbol{A}$ coefficient in Eq. (31) is identical to the SME coefficient $\tilde{\boldsymbol{b}}^e$ which contains contributions from *CPT*-violating as well as *CP*-violating terms [82]. The SME has terms similar to the $\boldsymbol{C}$ coefficients Eq. (33), expressed in sun-fixed coordinates.

The Ghost Condensate dynamical theory

A dynamical mechanism for the spontaneous breaking of Lorentz symmetry has been proposed by Arkani-Hamed and coworkers [83,84]. In their model, broken time-diffeomorphism symmetry creates a pervasive, massless, aether-like fluid consisting of Nambu–Goldstone bosons. Translational invariance requires a negative kinetic term in the Lagrangian, causing the bosons to form a "ghost condensate". Like a cosmological constant, the condensate does not dilute as the universe expands, and is therefore capable of accelerating the expansion rate of the universe. It defines a preferred frame that converges with the frame of the cosmic microwave background (CMB) as it reaches equilibrium. Cosmological tests of gravity limit the diffeomorphism symmetry-breaking scale M to be less than 10 MeV. If $M \sim 10^{-3}$ eV the condensate could drive the observed acceleration of the universe. If $M \sim 1$ eV it could mimic the observed dark matter.

The ghost condensate gives rise to two preferred frame effects that involve spin. First, a fermion moving with respect to the ghost condensate feels an interaction

$$V_G = \frac{M^2}{F} \boldsymbol{\sigma} \cdot \boldsymbol{v}/c, \tag{34}$$

where F is a mass scale associated with the coupling of the fermion to the condensate, and $\boldsymbol{v}$ is the fermion's velocity with respect to the condensate. Eq. (34) has the same form as Eq. (32).

Second, the ghost condensate can generate an interaction between two spins separated by $\boldsymbol{r}$

$$V_{GS}(\boldsymbol{r}, \boldsymbol{v}) = \frac{1}{8\pi} \frac{M^2}{F^2} (\boldsymbol{\sigma_1} \cdot \nabla)(\boldsymbol{\sigma_2} \cdot \nabla) \int \frac{\mathrm{d}^3 k}{(2\pi)^3} \frac{\mathrm{e}^{\mathrm{i}\boldsymbol{k} \cdot \boldsymbol{r}}}{M^2(\boldsymbol{v} \cdot \boldsymbol{k})^2 - k^4}, \tag{35}$$

where $\boldsymbol{v}$ is the relative velocity between the rest frame of the ghost condensate and the lab frame in which the spins are at rest.

When both spins are at rest with respect to the condensate or when one spin lies in the wake of the co-moving second spin [85,86] V_{GS} simplifies to

$$V_{GS}(\boldsymbol{r}, \boldsymbol{v} = 0) = \frac{1}{8\pi} \frac{M^2}{F^2} \frac{\boldsymbol{\sigma_1} \cdot \boldsymbol{\sigma_2} - (\boldsymbol{\sigma_1} \cdot \hat{\boldsymbol{r}})(\boldsymbol{\sigma_2} \cdot \hat{\boldsymbol{r}})}{r} \tag{36}$$

A search for V_{GS} requires both a spin pendulum and a spin source.

Non-commutative spacetime geometries

Preferred-frame effects can also arise in non-commutative space-time geometries [87,88], such as those associated with *D*-brane models. In these geometries, the space-time coordinates x_μ do not commute, but instead satisfy

$$\left[\hat{x}_\mu, \hat{x}_\nu\right] = \mathrm{i}\Theta_{\mu\nu}, \tag{37}$$

where $\Theta_{\mu\nu}$ is a real, antisymmetric tensor that has dimensions of length squared and $|\Theta|$ represents the smallest "observable" patch of area. To avoid problems with causality, it is often assumed that $\Theta_{0i} = 0$. If one also assumes that $\Theta_{\mu\nu}$ has been inflated, so that it is constant over the space-time region spanned by an experiment, then it defines a preferred direction $\eta^i = \epsilon^{ijk}\Theta_{jk}$. One consequence of Eq. (37) is that an electron experiences a *CP*-violating interaction [88,89]

$$\mathcal{L}_{\text{eff}} = \frac{3}{4} m \Lambda^2 \left(\frac{\alpha}{4\pi\hbar}\right)^2 \Theta^{\mu\nu} \bar{\psi} \sigma_{\mu\nu} \psi, \tag{38}$$

where Λ is a cutoff conventionally taken to be ∼1 TeV, and α is the fine structure constant. Eq. (38) is equivalent to

$$V_e = \boldsymbol{\sigma}_e \cdot \hat{\boldsymbol{\eta}} \left(\frac{\Lambda}{1\ \text{TeV}}\right)^2 3.33 \times 10^{36}\ \frac{\text{eV}}{\text{m}^2} |\Theta|, \tag{39}$$

which has the same form as Eq. (31).

4.1.2. Forces from unnatural-parity boson exchange

The virtual exchange of unnatural parity (pseudoscalar, axial vector, ...) particles produces spin-dependent forces that vanish between unpolarized bodies. Moody and Wilczek [90] discussed the forces produced by the exchange of low-mass, spin-0 particles and described two spin-dependent interactions. First, a pure pseudoscalar exchange would mediate a "dipole–dipole" interaction between two polarized electrons given by

$$V_{ee}(r) = \frac{g_{\mathrm{P}}^e g_{\mathrm{P}}^e\ \hbar^2}{16\pi m_{\mathrm{e}}^2 c^2}\left[(\boldsymbol{\sigma_1}\cdot\boldsymbol{\sigma_2})\left(\frac{1}{\lambda r^2}+\frac{1}{r^3}\right)-(\boldsymbol{\sigma_1}\cdot\hat{\boldsymbol{r}})(\boldsymbol{\sigma_2}\cdot\hat{\boldsymbol{r}})\left(\frac{1}{\lambda^2 r}+\frac{3}{\lambda r^2}+\frac{3}{r^3}\right)\mathrm{e}^{-r/\lambda}\right] \tag{40}$$

where $m_\phi = \hbar/(\lambda c)$ is the mass of the hypothetical spin-0 particle and g_{P} is its pseudoscalar coupling.

Second, the exchange of particles containing *CP*-violating $J^\pi = 0^+$ and $J^\pi = 0^-$ admixtures would produce a macroscopic, *CP*-violating "monopole–dipole" interaction between a polarized electron and an unpolarized atom with mass and charge numbers A and Z

$$V_{eA}(r) = g_{\mathrm{P}}^e g_{\mathrm{S}}^A \frac{\hbar}{8\pi m_e c}\boldsymbol{\sigma}_e\cdot\left[\hat{\boldsymbol{r}}\left(\frac{1}{r\lambda}+\frac{1}{r^2}\right)\mathrm{e}^{-r/\lambda}\right], \tag{41}$$

where g_{S} is its scalar couplings, and $g_{\mathrm{S}}^A = Z(g_{\mathrm{S}}^e + g_{\mathrm{S}}^p) + (A-Z)g_{\mathrm{S}}^n$.

Recently Dobrescu and Mocioiu [91] classified the kinds of potentials, constrained only by rotational and translational invariance, that might arise from the exchange of low-mass bosons. A spin pendulum is sensitive to 3 of their potentials. The first is a potential equivalent to Eq. (41). The two additional velocity-dependent potentials are given by

$$V_{eN}(r) = \frac{\boldsymbol{\sigma}_e}{8\pi}\cdot\left[f_\perp\frac{\hbar}{c}\frac{(\tilde{\boldsymbol{v}}\times\hat{\boldsymbol{r}})}{m_e}\left(\frac{1}{r\lambda}+\frac{1}{r^2}\right)+f_v\frac{\tilde{\boldsymbol{v}}}{r}\right]\mathrm{e}^{-r/\lambda}, \tag{42}$$

where $\tilde{\boldsymbol{v}}$ is the relative velocity in units of c. Both terms can be generated by one-boson exchange in Lorentz-invariant theories. The parity-conserving $f_\perp$ term can arise from scalar or vector boson exchange, while the parity-violating f_v term can be induced by spin-1 bosons that have both vector and axial couplings to electrons, giving $f_v = 2g_A^e g_V^N$.

4.1.3. Gravitational torsion

Intrinsic spin is a quantum mechanical property not included in the classical theory of general relativity. However if the Reimann geometry of general relativity is replaced by the more general Reimann–Cartan geometry, then an additional non-symmetric field called torsion appears [92]. Torsion does not directly couple to unpolarized matter, but it does couple to fermion spins. A spin pendulum that couples to a background torsion field [93,94] (assumed to be a constant field) results in a potential identical to Eq. (31). Torsion can also lead to gravitational spin–spin interaction

$$V_t(r) = (1+B)^2\,\frac{9\hbar^2 G}{8c^2}\,\frac{\boldsymbol{\sigma_1}\cdot\boldsymbol{\sigma_2}-3(\boldsymbol{\sigma_1}\cdot\hat{\boldsymbol{r}})(\boldsymbol{\sigma_2}\cdot\hat{\boldsymbol{r}})}{r^3} \tag{43}$$

where G is Newton's constant and B is a number that characterizes the deviation of the torsion coupling from that given by the minimally coupled Dirac equation [95].

4.2. Experimental issues

The central challenge for the detection of new weak spin-coupled forces is to isolate the spin interactions from the much larger magnetic background. Although a variety of techniques from atomic physics and low-temperature physics have been used to search for couplings to spin (for example, see Refs. [96–98]), we restrict our attention to torsion balance experiments that employ spin-polarized pendulums.

Phillips [99] used a transversely polarized permanent magnet suspended from a Kevlar fiber to search for an interaction of the form $g\boldsymbol{\sigma}\cdot\boldsymbol{v}$ where $\boldsymbol{v}$ is the velocity of the laboratory through inertial space. The torsion pendulum was placed inside a cryogenic chamber that contained both molypermalloy and superconducting shields to eliminate magnetic torques. A torque on the electron spins in the magnet with a period of one sidereal day was sought but not detected, corresponding to an upper limit on the splitting between the spin states of an electron of 8.5×10^{-18} eV.

Hou, Ni, and Li [100] constructed a tranversely-polarized pendulum, using ferrimagnetic $\mathrm{Dy_6\,Fe_{23}}$. In this compound, the magnetic moments of the polarized Fe electrons spins are largely canceled by the orbital magnetic moments of the Dy atoms. The resultant magnetization varies with temperature, crossing zero near room temperature. The 29 g of $\mathrm{Dy_6\,Fe_{23}}$ was encased within 39 g of magnetic shielding to produce a pendulum with a residual magnetic dipole moment of 2.5×10^{-2} erg/G. Hou et al. estimated that their pendulum contained 8.95×10^{22} polarized electrons, corresponding to roughly 0.4 polarized electron per atom of $\mathrm{Dy_6\,Fe_{23}}$. The $\mathrm{Dy_6\,Fe_{23}}$ pendulum was suspended within a μ-metal shield and external Helmholtz coils held the field outside the μ-metal below 2 mG. The torsion balance apparatus was mounted on a turntable that rotated with a one hour period; a torque on the pendulum spins from a constant background field would produce a sinusoidal twist of the pendulum with a frequency equal to the turntable rotation frequency. Hou et al. analyzed their data for an interaction

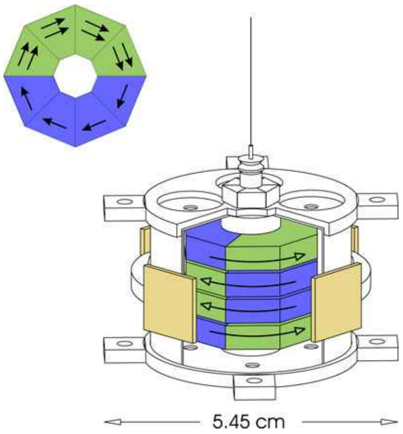

Fig. 14. Scale drawing of the EW spin pendulum. The light green and darker blue volumes are Alnico and Sm Co_5, respectively. Upper left: top view of a single "puck"; the spin moment points to the right. Lower right: the assembled pendulum with the magnetic shield shown cut away to reveal the 4 pucks inside. Two of the 4 mirrors (light gold) used to monitor the pendulum twist are prominent. Arrows with filled heads show the relative densities and directions of the electron spins, open-headed arrows show the directions of $\boldsymbol{B}$. The 8 tabs on the shield held small screws that we used to tune out the pendulum's residual q_{21} gravitational moment. (For interpretation of the references to colour in this figure legend, the reader is referred to the web version of this article.)

Table 6
1σ constraints from EW and from Hou et al. [100] on the Lorentz-violating rotation parameters defined in Eq. (31)

Parameter	EW	Hou et al. [100]
A_X	-0.67 ± 1.31	-108 ± 112
A_Y	-0.18 ± 1.32	-5 ± 156
A_Z	-4 ± 44	107 ± 2610

Units are 10^{-22} eV. The errors in A_Z are larger than those in A_X and A_Y because of the greater systematic uncertainty in lab-fixed signals. It is assumed that C terms can be neglected.

of the form given by Eq. (31), and achieved the best upper limit on coupling to electron spin at that time, shown in Table 6. The combination of a self-shielding pendulum, external magnetic shields, Helmholtz coils, and a rotating apparatus reduced magnetic interactions to a tolerable level.

The most recent experiment with a spin pendulum was performed by the Eöt–Wash group (EW) [101,102]. In this work, a self-shielding pendulum, shown in Fig. 14 was constructed from two permanent magnet materials with different spin contributions to the net magnetization. The EW spin pendulum was constructed from 4 octagonal "pucks". One half of each puck was Alnico 5 (a conventional, relatively "soft" ferromagnet in which the magnetic field is created almost entirely by electron spins) and the other half was grade 22 Sm Co_5 (a "hard" rare-earth magnet in which the orbital magnetic moment of the electrons in the Sm^{3+} ion nearly cancels their spin moment [103–105]). The trapezoidal elements of the pucks were fabricated by electric-discharge machining, and kept in precise alignment by aluminum frames. Thin plates glued to the sides of the Alnico pieces compensated for their lower density, $\rho = 7.37$ g/cm^3 versus 8.3 g/cm^3 for Sm Co_5. After each puck was assembled, the Alnico was magnetized to the same degree as the Sm Co_5 by monitoring the external B fields as appropriate current pulses were sent through coils temporarily wound around the pucks. By stacking 4 such pucks as shown in Fig. 14, the effective center of the spin dipole was placed in the middle of the pendulum, small density differences between Alnico and Sm Co_5 were averaged away, and the composition dipole that would have made the pendulum sensitive to a violation of the weak Equivalence Principle was canceled.

The pucks were surrounded by a gold-coated μ-metal shield that supported 4 mirrors equally spaced around the azimuth. The 64 g of magnets inside of the shield produced a pendulum with a residual magnetic dipole moment of 7×10^{-3} erg/G and as discussed below, a measured net spin dipole of $(9.80 \pm 0.22) \times 10^{22}$ polarized electrons.

The EW spin pendulum was surrounded by 4 layers of magnetic shielding and Helmholtz coils. The apparatus was mounted on a turntable that rotated with a period of approximately 20 min. To distinguish torques acting on the pendulum spins (which produced twist signals at the turntable rotation rate) from reproducible signals arising from imperfections in the turntable rotation rate, the orientation of the pendulum relative to the turntable was cycled through each of 4 positions, defined by which mirror reflected light to the twist monitoring system.

Because the pendulum's magnetic flux was confined entirely within the pucks, the stationary pendulum necessarily contained a net total angular momentum $\boldsymbol{J} = -\boldsymbol{S}$, where $S = N_p\hbar/2$ is the pendulum's net spin:

$$\langle M_z^{\rm tot}\rangle = 2\langle S_z^{\rm tot}\rangle + \langle L_z^{\rm tot}\rangle = \langle S_z^{\rm tot}\rangle + \langle J_z^{\rm tot}\rangle = 0, \tag{44}$$

after making the excellent approximation that $g_s = 2$.

Table 7
1σ constraints on the C parameters of Eq. (33)

Parameter	Value	Parameter	Value
C_{XX}	$+0.96 \pm 2.16$	C_{YX}	-3.74 ± 2.17
C_{XY}	$+1.84 \pm 4.24$	C_{YY}	-7.76 ± 4.25
C_{XZ}	-3.92 ± 10.16	C_{YZ}	$+16.17 \pm 10.23$
C_{ZX}	-4.92 ± 8.86		
C_{ZY}	-9.6 ± 20.9		
C_{ZZ}	$+24.8 \pm 43.9$		

The last three rows in this table are inferred from lab-fixed measurements. Units are 10^{-18} eV.

To keep $\boldsymbol{J}$ fixed in the frame of the rotating earth, the torsion fiber had to apply a steady torque, $\boldsymbol{T}$, given by

$$\boldsymbol{T} \cdot \hat{\boldsymbol{n}} = (\boldsymbol{\Omega}_{\oplus} \times \boldsymbol{J}) \cdot \hat{\boldsymbol{n}}, \tag{45}$$

where $\boldsymbol{\Omega}_{\oplus}$ is the sidereal rotation frequency and $\hat{\boldsymbol{n}}$ is the local vertical. The pendulum twisted until $\kappa\theta = -\boldsymbol{T} \cdot \hat{\boldsymbol{n}}$, i.e. $\boldsymbol{J}$ tried to point toward true North, like a gyro-compass, with a torque

$$\boldsymbol{T} \cdot \hat{\boldsymbol{n}} = N_{\mathrm{p}} \frac{\hbar \boldsymbol{\Omega}_{\oplus} \cos \Psi}{2} = N_{\mathrm{p}} \times (2.590 \times 10^{-39}\ \mathrm{N\ m}), \tag{46}$$

where $\Psi = 47.66$ deg is the latitude of the EW lab.

The EW team measured a constant torque on the spin dipole of their pendulum of (0.254 ± 0.006) fN m that pointed to within 1.4 ± 1.5 deg of true South and interpreted this torque as the gyro-compass torque [102]. This measurement provided a calibration of the number of polarized spins in the pendulum, given above.

4.3. Results and implications

The EW team collected spin-pendulum data over a four-year period and recently reported results for many of the potentials given above [102]. They adopted Cartesian equatorial coordinates for their inertial frame, where $\hat{\boldsymbol{Z}}$ points North along the earth's spin axis, $\hat{\boldsymbol{X}}$ points from the earth to the sun at the 2000 vernal equinox, and $\hat{\boldsymbol{Y}} = \hat{\boldsymbol{Z}} \times \hat{\boldsymbol{X}}$. Astronomical sources that had a projection onto the $\hat{\boldsymbol{X}}\hat{\boldsymbol{Y}}$ plane produced torques that were modulated daily, while sources aligned along $\hat{\boldsymbol{Z}}$ produced constant ("lab-fixed") torques.

4.3.1. Lorentz symmetry violation

Upper limits on rotational invariance (the potential given in Eq. (31)) are given in Table 6.

Taking $\boldsymbol{v}$ as the velocity of the spin pendulum relative to the CMB rest frame, the UW group found a 1σ upper limit on the boost-violating potential in Eq. (32) of

$$B = (+0.50 \pm 1.13) \times 10^{-19}\ \mathrm{eV}. \tag{47}$$

Table 7 displays the EW limits on the electron's generalized helicity tensor $\boldsymbol{C}$. We are not aware of any comparable measurements of either B or C for electrons, but similar limits on C for neutrons are given in Ref. [96].

The result in Eq. (47) provides a limit on the ghost condensate coupling $-M^2/F$ (see Eq. (34)) of

$$\frac{M^2}{F} = (-0.50 \pm 1.10) \times 10^{-19}\ \mathrm{eV}, \tag{48}$$

which improves on the value given in Ref. [84] by three orders of magnitude. The corresponding 95% confidence constraint on the "ghost condensate parameter" M/F is shown as a function of M in Fig. 15. A condensate-mediated spin–spin interaction with a strength comparable to gravity would have the ghost condensate parameter $M/F \sim 10^{-16}$ [84].

Inserting the constraint on $|\boldsymbol{A}|$ from Table 6 into Eq. (39), gives an 1σ upper limit on $|\Theta|$, the minimum observable patch of area of a non-commutative geometry,

$$|\Theta_{XZ}|\ \text{or}\ |\Theta_{YZ}| \leq 4.9 \times 10^{-59}\ \mathrm{m}^2\ [1\ \mathrm{TeV}/\Lambda]^2 \tag{49}$$

$$|\Theta_{XY}| \leq 1.5 \times 10^{-57}\ \mathrm{m}^2\ [1\ \mathrm{TeV}/\Lambda]^2 \tag{50}$$

which, assuming $\Lambda = 1$ TeV, corresponds to energy scales of 2.8×10^{13} GeV for Θ_{XZ} or Θ_{YZ} and 5.0×10^{12} GeV for Θ_{XY}.

4.3.2. Forces from boson-exchange

The constraints on CP-violating monopole–dipole interactions of Eq. (41) with $\lambda \geq 1$ cm extracted from the lab-fixed and solar-source data are shown in Fig. 16 (see also Table 8). This new work improves over previous work [106,98,107] by factors of up to 10^4.

The limits on velocity-dependent boson-exchange forces, extracted from the experimental bounds on interactions between the spin pendulum and the sun, are given in Table 8. Fig. 17 shows range-dependence of the velocity-dependent couplings f_v and $f_\perp$. We are not aware of any previous measurements of such forces.

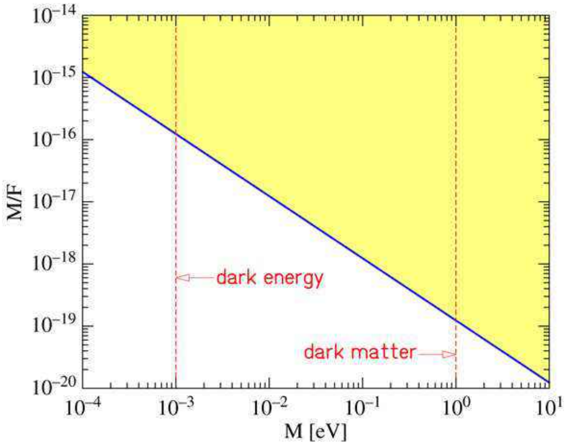

Fig. 15. Upper limits on the "ghost condensate" parameter M/F as a function of M. The shaded area is excluded at 95% confidence. The vertical dashed lines show values of M having particular cosmological significance.

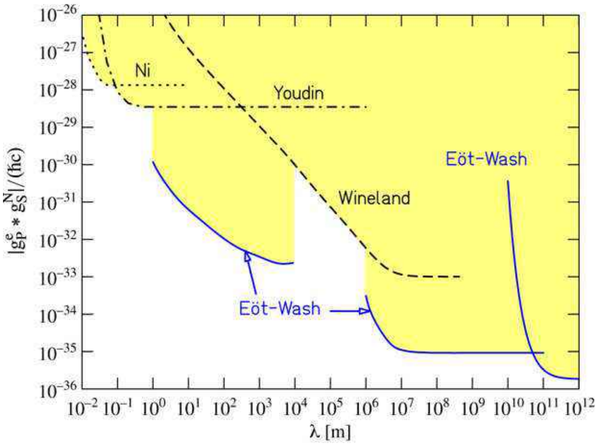

Fig. 16. Upper limits on $|g_P^e g_S^N|/(\hbar c)$ as a function of interaction range λ; the shaded region is excluded at 95% confidence. The Eöt–Wash results and previous work by Youdin et al. [106], Ni et al. [98] and Wineland et al. [107] are indicated by solid, dash-dotted, dotted and dashed lines, respectively.

Table 8
1σ boson-exchange constraints from interactions with the Sun and Moon

Parameter	Solar constraint	Lunar constraint
$g_P^e g_S^N/(\hbar c)$	$(-3.5 \pm 8.5) \times 10^{-37}$	$(+0.2 \pm 1.6) \times 10^{-34}$
$f_\perp/(\hbar c)$	$(-0.1 \pm 2.1) \times 10^{-32}$	$(-1.1 \pm 8.6) \times 10^{-29}$
$g_A^e g_V^N/(\hbar c)$	$(+0.2 \pm 1.2) \times 10^{-56}$	$(-3.1 \pm 2.4) \times 10^{-50}$

Note that $f_v = 2g_A^e g_V^N$. The solar and lunar constraints assume $\lambda \gg 1.5 \times 10^{11}$ m and $\lambda \gg 4 \times 10^{8}$ m, respectively.

4.4. Future prospects

Spin pendulum tests of preferred-frame effects have achieved experimental sensitivities comparable with the best allowed by state of the art torsion balance technology. Modest improvements in the spin density of the pendulum and the sensitivity of the torsion balance apparatus may be anticipated, but large improvements are not foreseen. Tests for exotic boson exchange will continue, pushing to ever smaller distance scales.

A promising avenue of research is the construction of spin attractors and pendulums to probe the spin–spin interactions of Eqs. (35), (40) and (43). A first-generation experiment of this type was recently completed at the EW group [86], and a second generation experiment is in progress. Because many of the spin–spin potentials die off as $1/r^3$, it is advantageous to place the spin source as close as possible to the spin pendulum. An experiment that combines the technologies of self-shielding spin sources with those of the short-distance test of the inverse square law is being developed by the EW group.

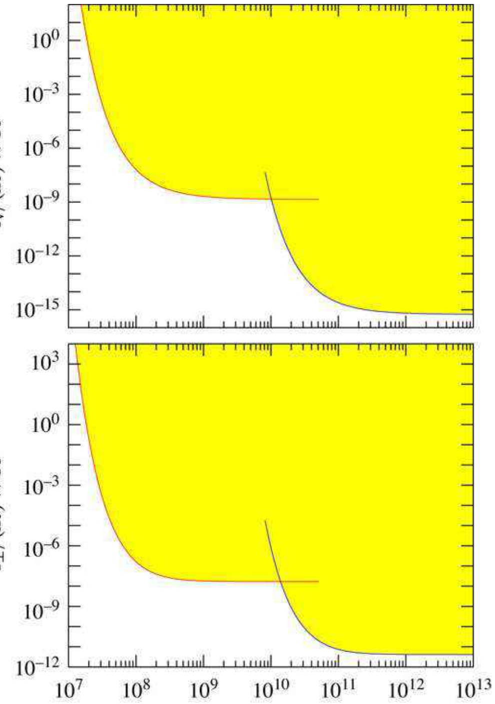

Fig. 17. Constraints on the velocity-dependent couplings f_v and $f_\perp$ inferred from the infinite-range results in Table 8. The shaded area is excluded at 95% confidence. In making this plot from the $\lambda = \infty$ results in Table 8 the eccentricities of the earth's and moon's orbits were neglected.

5. Monopole–dipole searches for axion-like particles

5.1. Motivation

A wide variety of extensions to the Standard Model predict new pseudoscalar bosons that are typically the pseudo-Nambu–Goldstone bosons of spontaneously broken symmetries, such as familons [108], majorons [109,110], arions [111], omions [112] or axions [113,114]. Pseudoscalars can also arise in the context of technicolor [115], superstring [116,117] and Kaluza–Klein [118,119] theories.

The axion, the pseudo-Nambu–Goldstone boson of a hypothesized U(1) Peccei-Quinn (PQ) global symmetry, is the most studied pseudoscalar with several searches actively underway. The axion is a particularly attractive concept, because the addition of PQ symmetry to the standard model provides an elegant solution to the so-called "Strong-CP" problem [120,121]: *i.e.* the QCD Lagrangian explicitly breaks CP symmetry, but the CP-violating parameter, Θ_{QCD}, is constrained to be less than $\sim 10^{-10}$ by bounds on the electric dipole moment of the neutron [122,123] and the Hg atom [124]. The axion field, generated by the spontaneous breaking of PQ symmetry at a high energy scale, f_a, dynamically minimizes CP violation to a very small value. In all axion models the mass is uniquely determined by the energy breaking scale, $m_a \sim 6\ \mu\text{eV}\ (10^{12}\ \text{GeV}/f_a)$. The exact coupling of the axion to fundamental fermions and photons, however, is somewhat model dependent. Two axion models are commonly discussed in the literature: the "hadronic" or KSVZ axion [125], in which the axion couples at tree level only to a super-heavy, as yet unobserved, quark; and the "GUT" scale, or DFSZ axion [126], in which the axion couples to all quarks and leptons. In both models, aside from order unity model-dependant parameters, the axion coupling scales as $1/f_a$. Thus, the PQ axion's coupling constants are directly proportional to its mass. For other pseudoscalars, this relationship between the particle's mass and interaction strength does not necessarily hold; for this reason all other pseudoscalars are typically referred to as axion-like particles or ALPs in the literature. For an up-to-date and comprehensive review of axion physics see [127].

Although accelerator-based experiments provided early constraints on axions and ALPS, through limits on decays like $K^+ \to \pi^+ +$nothing [128], the best current constraints are set by cosmology and astrophysics. If the axion were sufficiently light, too many axions would have been created as the universe cooled and over-closed the universe. The exact bound this places on the axion depends strongly on the cosmological model, the energy scale of inflation, and the re-heat temperature after inflation. Nevertheless, recent cosmic-microwave background observations suggest $m_a > O\ (10\ \mu\text{eV})$ [129,130]. If the axion were sufficiently heavy, it would provide a substantial cooling channel for stars and supernova. Measurements and models of the neutrino pulse generated by SN1987A thus constrain $m_a < 0.01$ eV [131]. (N.B. These limits do not strictly apply to ALPS; they must be evaluated for each model individually). These limits define the so-called "axion-window." Within this window, the axion is an ideal dark matter candidate. Relic axions, created as the early universe cooled through the PQ symmetry breaking scale, would today be cold, abundant, non-baryonic, and very weakly interacting. Generically, the axion density, Ω_a, scales as $(1/m_a)^{(7/6)}$. Thus, if the axion is on the light side of the axion window, it could be the principal component of dark matter; if the axion is on the heavy side, it could be one of many dark matter particles.

Axions or ALPs whose mass is within or lighter than the axion window will mediate macroscopic forces that may be detected with laboratory-scale torsion balances. For instance, axions within the "axion-window" would mediate forces with a characteristic range between 0.002 cm and 2.0 cm. Any pseudoscalar can interact with fundamental fermions, either through a scalar or pseudoscalar vertex. As Moody and Wilczek recognized, they can mediate three different macroscopic potentials [90]: the dipole–dipole and monopole–dipole of Eqs. (40) and (41), respectively, and a monopole–monopole potential

$$V(\vec{r}) = \frac{g_s^1 g_s^2 e^{-r/\lambda}}{4\pi r}. \tag{51}$$

Note that the scalar couplings g_S in Eqs. (41) and (51) only occur in models with residual CP violation. For axions, this CP-breaking admixture is provided by the very small, but finite, CP violation in the QCD Lagrangian. Thus, in these models one expects $g_s \propto \Theta_{QCD}$. In ALP models, g_s could be proportional to another CP violating parameter. Alternatively, an ALP model could respect CP symmetry, in which case the ALP would not mediate a monopole–dipole or monopole–monopole force. In axion models, one does not expect CP violation in the lepton sector, and thus, g_s is typically assumed to be the coupling to unpolarized nucleons only. Any axion or ALP model will couple via the pseudoscalar vertex, which can be with polarized electrons, g_p^e, or polarized nucleons, g_p^N.

The monopole–monopole potential is a challenge, because it scales as g_s^2. The dipole–dipole force does not depend on any CP violation, a big advantage for experiments looking for this potential. Constraining this force, however, may be difficult because for long wavelength (low mass) ALPs, the potential over laboratory scales will mimic the magnetic dipole–dipole interaction. Although the monopole–dipole interaction scales with one power of g_s, it is perhaps not as daunting as the dipole–dipole force: the monopole–dipole potential is unlike any known macroscopic force in nature: it violates both parity and time-reversal symmetries. A positive discovery would be the first evidence for macroscopic violation of either symmetry.

5.2. *Current constraints*

5.2.1. *Direct searches*

The ADMX collaboration is looking for the conversion of dark matter axions into detectable photons in a resonant microwave cavity pervaded by a magnetic field. This impressive experiment has excluded KSVZ axions with a mass between 1.9 and 2.3 μeV as the principle component of dark matter, if they are virialized in the gravitational field of our galaxy [132]. ADMX has also excluded DFSZ axions with a mass between 1.98 and 2.17 μeV if they are *not* virialized [133]. A near term detector upgrade should enable ADMX to also conclusively exclude DFSZ axions that are virialized. However, axions can not be conclusively excluded by the present version of ADMX. Axions may be much heavier; in fact, given the recent WMAP measurements of the cosmic microwave background, a heavy ($m_a \sim 100$ μeV) axion is preferred in some cosmologies [134, 135]. To search for such a heavy axion ADMX will need to employ numerous, much smaller microwave cavities than at present. The axion may also not be the principal component of dark matter. Finally, in some models it is possible that axion-photon coupling is suppressed at tree level [136]. Other efforts, with far less sensitivity than ADMX, also rely on the axion-photon coupling. The CAST collaboration [137] is using a decommissioned LHC magnet to look for axions radiated by the sun. Inspired by a recent result [138] of the PVLAS group suggesting the discovery of an ALP (now excluded by an experiment upgrade [139]), a number of groups world-wide are attempting to "shine light through walls" to constrain ALPs [140].

5.2.2. *Monopole–dipole searches*

Macroscopic-force searches for axions and ALPs complement other axion search efforts. Monopole–dipole force searches are limited by the small value of Θ_{QCD}, which makes their present sensitivity small compared to ADMX. On the other hand, over a broad mass range, they place hard limits on the scalar and pseudoscalar vertex couplings of *any* light pseudoscalar.

Over the past two decades, numerous efforts have been undertaken to constrain $g_s g_p^{(n)}$ and $g_s g_p^{(e)}$. Baessler et al. [141] provide the best limits on $g_s g_p^{(n)}$ at very short ranges, by observing the transmission of ultra-cold neutrons (UCN) through a very narrow volume between two glass plates. Because the UCN wavelength is comparable with the gap between the plates, the probability that an UCN will transit this volume is very sensitive to a new force between the neutron and the plates. At much greater distances, the best constraints are obtained by looking for a difference in the precession frequency of a Hg magnetometer between two orientations of a magnetic field, with reference to the gravitational field of the earth [142] or a pair of 475 kg lead masses [106].

The best long-range constraints on $g_s g_p^{(e)}$ are provided by the Eöt–Wash spin-pendulum [101], discussed in Section 4 of this review. Over a limited range, between 10^4 and 10^6 m, where the source integral is uncertain for the Eöt–Wash work, the best limit is set by Wineland et al. [107], who studied the change in the hyperfine splitting of $^9\text{Be}^+$ ions when an external field was applied parallel or anti-parallel with the Earth's gravitational field. Within the axion window, for the longest ranges, Ni et al. [98] provide the best bound by testing if the presence of a 1 kg copper mass can polarize a paramagnetic salt. Hammond

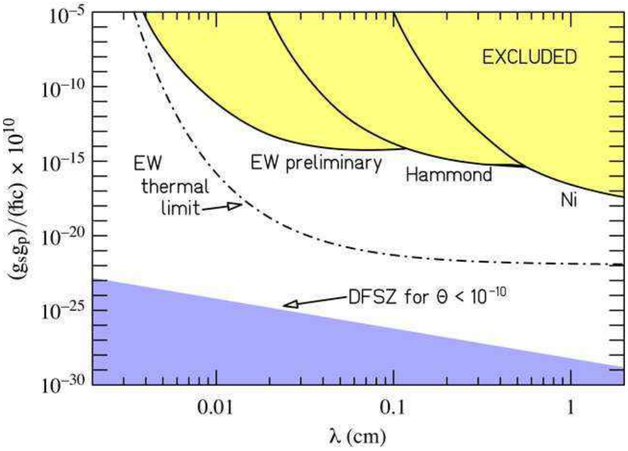

Fig. 18. Current and prospective bounds on the monopole–dipole force. Experiments by Ni et al. [98], Hammond et al. [143] and preliminary Eöt–Wash results by Hoedl et al. [144] exclude the upper shaded region at 95% confidence. The dashed curve shows the ultimate sensitivity of the current Eöt–Wash instrument if systematic effects could be eliminated. The lower shaded region shows the expected DFSZ axion signal assuming that $\Theta_{QCD} \leq 10^{-10}$.

et al. [143] provide the most restrictive published limits on $g_s g_p^{(e)}$ at the shortest ranges. They employed a magnetically levitated torsion pendulum to directly look for a force between the electrons in a polarized, cylindrical mu-metal shield, and unpolarized nucleons in copper rods suspended inside the mu-metal.

5.3. The Eöt–Wash ALP pendulum

The EW group is commissioning a new torsion pendulum that will place the best constraints on $g_s g_p^{(e)}$ at the heavy mass end of the axion window. The torsion pendulum consists of a laser-cut, 500 μm thick, gold-coated, single-crystal silicon wafer. The pendulum is suspended by a 0.7mil thick, 1m long, tungsten fiber, between two halves of a split toroidal electromagnet, which is fixed in place and cannot move (see Fig. 19). As in our other experiments, the pendulum angle is read with a custom built auto-collimator. The electromagnet serves as the source of polarized electrons; the silicon wafer is the source of unpolarized nucleons. If there exists a monopole–dipole force, the silicon wafer will experience a torque proportional to the field strength of the magnet. Thus, if $g_s g_p^{(e)} > 0$, the pendulum will feel a counterclockwise torque if the magnetic field is clockwise and a clockwise torque if the field is counterclockwise. If this pendulum operated with thermal noise as the only source of statistical error (with no systematic errors), its sensitivity to a monopole–dipole force would be unprecedented. Fig. 18 shows the thermal noise limit if the pendulum is operated for 100 days with a field of 10 kG and a magnet-pendulum separation of 100 μm.

As one can see in Fig. 19, parts of the silicon wafer are in a strong magnetic field. Thus, the Eöt–Wash ALP pendulum is subject to systematic and statistical sources of error associated with the magnetic field, in addition to the sources of noise which effect other torsion pendulums. Clearly, ferromagnetic impurities in the silicon could be responsible for torque on the pendulum that is linear in the applied magnetic field. To minimize the ferromagnetic impurities, the pendulum is made of zone-refined silicon, which is pure to better than 1 part in 10^{10}. We also employ a rigorous cleaning procedure to minimize surface impurities. In addition, one can always move the pendulum closer to one pole face or another. A signal due to fixed ferromagnetic impurities will not depend on the pendulum position, only the field strength. A signal due to an ALP, however, will show a strong dependence on the distance between the pendulum and the electromagnet pole face. If a signal were to be observed, this dependence would also measure the ALP mass.

The finite magnetic susceptibility of silicon ($\chi_m = -2.6 \times 10^{-7}$) is responsible for interesting effects. The potential energy of the pendulum in the magnetic field (in cgs units) is

$$U = \frac{\chi_m}{8\pi} \int B^2(\boldsymbol{r}, \theta) \mathrm{d}^3\boldsymbol{r} \tag{52}$$

where the integral is taken over the whole pendulum volume, and θ is the pendulum angle. Because silicon is diamagnetic, the pendulum will seek the field minimum. For small rotations about this minimum, one expects

$$B(\vec{r}, \theta) = B_0(\boldsymbol{r})(1 + c(\boldsymbol{r})(\theta - \theta_0(\boldsymbol{r}))^2) \tag{53}$$

where $c(\boldsymbol{r})$ is a dimensionless measure of the field's curvature, and $\theta_0(\boldsymbol{r})$ accounts for the fact that if the magnet halves are not perfectly aligned, for each small region of the pendulum, the magnetic field is minimized at a slightly different pendulum angle. The magnetic field, therefore, acts as an effective torsional spring with a spring constant $\kappa = (\chi_m/2\pi) \int B_0^2(\boldsymbol{r}) c(\boldsymbol{r}) \mathrm{d}V$. The magnetic field curvature is greatest near the magnet pole face edges. The silicon wafer was cut so that a minimum of

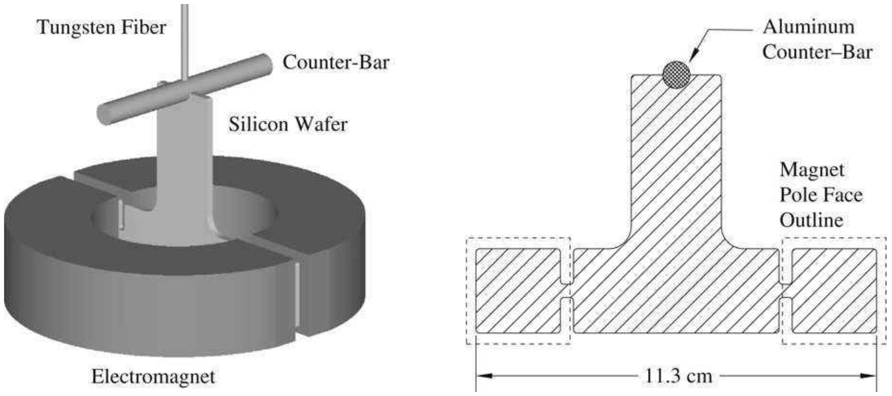

Fig. 19. Eöt–Wash ALP pendulum. Left image shows pendulum suspended between the two electromagnet halves. The right image shows a face-on view of the pendulum with the magnet pole face outlined.

material was located in these regions (see Fig. 19). Nevertheless, the magnet spring is very strong compared with the torsion fiber. Currently, at a field strength of ∼4 kG the magnet spring is ∼500 times stronger than the torsion fiber.

Advantage is taken of the magnetic spring in the following manner. The magnet is slowly energized to a constant current, and the pendulum motion recorded for an integral number of pendulum periods. An electrostatic feedback system which holds the pendulum at a fixed angle is turned on, while the current is slowly ramped to the opposite sign. Feedback prevents induced currents in the gold coating on the silicon from exciting the pendulum during magnet transitions. After a brief delay, the feedback is switched off and the pendulum motion is again recorded for an integral number of periods. This cycle is then repeated multiple times. For each constant current state the average pendulum position is calculated. An ALP signal is the difference between the average position in the magnet clockwise state and counterclockwise state.

The finite susceptibility of the silicon wafer can generate a false effect in several ways. First, if the absolute magnitude of the field is different in the two magnet states, then the magnet spring constant will also be slightly different. If there is another torque on the pendulum, which does not change when the magnet state is changed, the equilibrium angle will be slightly different in the two magnet states and a false effect will be observed. There are many sources of torque acting on the pendulum. For instance, a slight twist in the torsion fiber or near-by electric charges will create a torque. For this reason, a careful degauss procedure was developed to make the magnet spring as symmetric as possible. In addition, any changes in the pendulum period probe for effects due to slight differences in the magnetic spring constant.

A fixed magnet field gradient can also generate a false effect. In this case,

$$B(\boldsymbol{r},\theta) = B_0(\boldsymbol{r})(1 + c(\boldsymbol{r})(\theta - \theta_0(\boldsymbol{r}))^2) + \frac{\partial B_f(\boldsymbol{r})}{\partial \theta}(\theta - \theta_f(\boldsymbol{r})). \tag{54}$$

To first order, the equilibrium angle of the pendulum is then given by solving:

$$\frac{\partial U}{\partial \theta} = 0 = \frac{\chi_m}{8\pi} \int 4c(\boldsymbol{r})B_0^2(\boldsymbol{r})(\theta - \theta_0(\boldsymbol{r})) + B_0(\boldsymbol{r})\frac{\partial B_f(\boldsymbol{r})}{\partial \theta}\mathrm{d}^3\boldsymbol{r}. \tag{55}$$

Clearly, a field gradient, which does not change sign when the magnetic field changes sign, will make the equilibrium position slightly different in the two magnet states. The gradient will not change the magnetic spring constant, and thus, this effect mimics an ALP signal. A field gradient could be the result of external laboratory fields. Thus, the pendulum is placed within a magnetic shield. A fixed field gradient could also be the result of a slight asymmetry between the magnet halves. If a small region of one magnet is magnetically hard, so that it does not flip direction with the rest of the magnet iron, a gradient between the magnet halves will be created. It may be possible to minimize the effects of the silicon susceptibility by coating the pendulum with a thin layer of a highly paramagnetic material, such as Terbium ($\chi_m = 9 \times 10^{-3}$).

At present, the uncertainty in the Eöt–Wash ALP result is dominated by scatter induced by the degaussing procedure. The equilibrium asymmetry between magnet states changes after each degauss. The source of this scatter is currently under investigation. Nevertheless, given this source of error, preliminary exclusion bounds on a monopole–dipole force are 10^{10} times better than [143] at $\lambda = 200$ μm (see Fig. 18).

6. Experimental considerations in torsion balance technology

6.1. Torque read-out methods

Torsion-balance torques are measured using several techniques: by measuring the twist angle of a free pendulum with a position-sensitive detector [11,145,12], by nulling the torque with a feedback scheme [19] as discussed below, or by inferring the torque from a change in the pendulum's free period [146] or the induced harmonics in its motion [147].

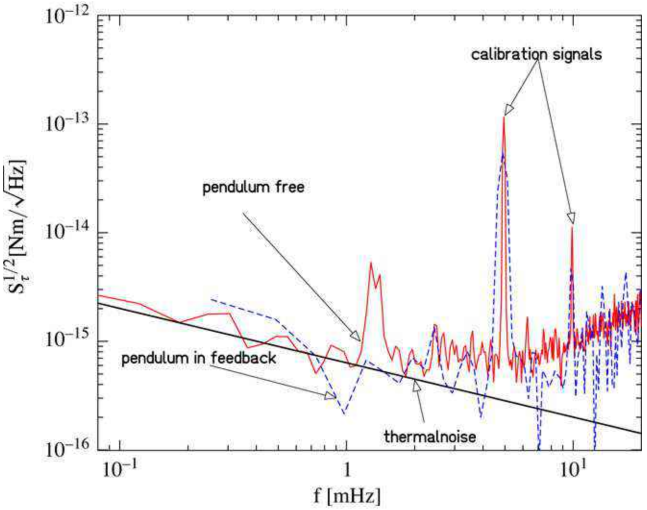

Fig. 20. Power spectral density of the twist signal from a torsion balance in the free (solid line) and in electrostatic feedback (dashed line) modes [152]. In both cases, the balance operates near the thermal limit (straight line) below ≈1 mHz, while at higher frequencies the autocollimator noise dominates. The sharp peaks at 5 and 10 mHz are an applied gravitational calibration torque.

In most torsion balances, the twist angle is monitored by an optical autocollimator, in which light from a small laser diode or LED is made into parallel beam using a lens. This parallel beam is reflected once or more times off the pendulum and returned through the same optics and directed onto a position-sensitive detector. The sensitivity of the autocollimator system can be as good as a few nrad/$\sqrt{\text{Hz}}$. In most autocollimator designs the angle noise scales with the dynamic range. Cowsik et al. are developing an autocollimator that images an array of slits onto a CCD-array. Pattern-recognition software gives their autocollimator sub-nanorad sensitivity, while maintaining an exceptionally large linear range [148].

When extracting the pendulum torque $\tau(f)$ from twist-angle measurements, the dynamical response of the pendulum must be taken into account. A torque at the frequency f causes a complex deflection amplitude

$$\phi(f) = \frac{1/\kappa}{(1 - f^2/f_0^2) + \mathrm{i}/Q}\tau(f), \tag{56}$$

where f_0 is the natural frequency of the pendulum, κ is the torsional constant and Q is the torsion oscillator's mechanical quality factor. This response function must be unfolded from the data to recover the torques of interest.

In the feedback technique [19], the autocollimator signal becomes the input sensor to a proportional-integral-differential-loop that controls voltages on small electrodes near the pendulum. These electrodes apply a torque that cancels the external torque, so that the autocollimator signal remains unchanged and the voltages are used to infer the external torque on the pendulum. In most electrode configurations the applied torque is proportional to V^2. To linearize the torque, it is often practical to operate one electrode at a constant voltage and use the opposite electrode as the control element. It is important that a low-noise autocollimator is used as the autocollimator noise is also amplified. Fig. 20 shows the torque extracted in both the free-running and feedback modes. Gundlach and Merkowitz, in their measurement of Newton's constant, used a torque feedback scheme first employed in Ref. [149], in which the rotation rate of the turntable containing the balance is varied so that the torsion fiber remains untwisted [150].

In the period-change method, the pendulum is given a relatively large amplitude as it oscillates in the restoring potential of the torsion fiber and the external force of interest. Any change in the external force, say by rotating an attractor around the pendulum, produces a small, but precisely measurable, frequency change. This method was commonly used in measuring the gravitational constant and has recently been refined by Newman and Boynton [151]. Boynton et al. have developed a technique that does not require a moveable attractor. Their torsion pendulum oscillates through several revolutions and the signal is detected as a non-harmonic content in the torsion angle. The large deflection amplitudes greatly exceed the dynamic range of an autocollimator. Boynton et al. extract the angle of their pendulum by timing light beams reflected from a polygonal mirror on the pendulum [147].

6.2. Statistical noise sources

6.2.1. Thermal noise

Dissipative thermal effects set a fundamental limit to the sensitivity of torsion-balance experiments [153]. Two distinct damping mechanisms, gas or eddy-current drag and internal losses in the suspension fiber, can affect the torsion oscillator. Gas damping and eddy-current damping, which give a white spectrum of torque noise, can easily be made negligible. Fig. 21

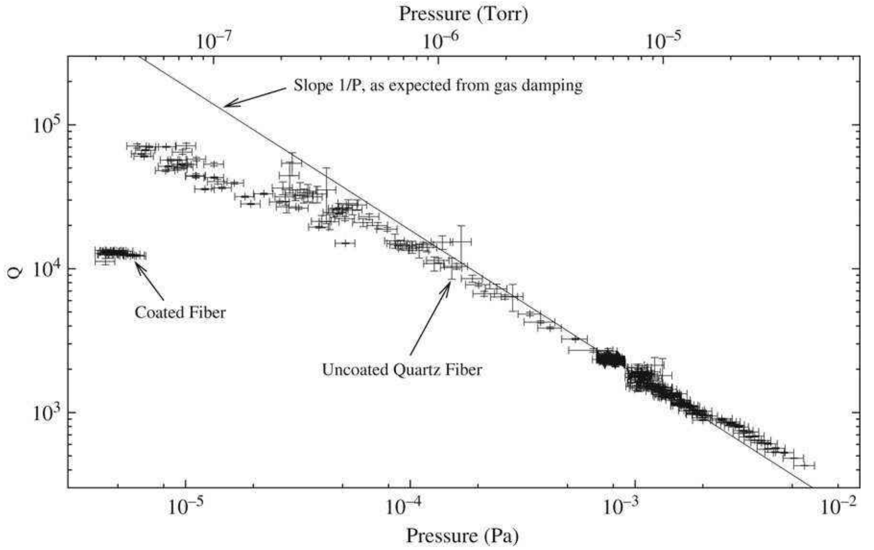

Fig. 21. Mechanical Q of a torsion pendulum and quartz fiber as a function of residual pressure [143]. An uncoated fiber was used for most of the the data; applying a thin metallic coating to the fiber reduced its Q to about 10^4. Note that a pressure of 10^{-4} Pa is sufficiently low that the dominant noise source in a tungsten fiber with an internal Q of 4000 would be the losses in the fiber itself.

shows the noise of a torsion balance as a function of gas pressure. At pressures for which the mean free path of gas molecules is longer than the typical distance between the pendulum and nearby surfaces, gas damping rapidly becomes unimportant. Most modern torsion balances are operated at pressures below 10^{-4} Pa, with the vacuum maintained by an ion pump or a turbo-molecular pump. On the other hand, internal losses in the material of the suspension system typically dominate and produce a frequency-dependent torque noise [153]

$$S_\tau^{1/2}(f) = \sqrt{\frac{4k_BT\kappa}{2\pi Qf}}, \tag{57}$$

where k_B is Boltzmann's constant, and κ and T are the torsion constant and temperature of the torsion fiber, respectively. Thermal noise is minimized by reducing κ/Q of torsion oscillator, modulating the signal at a high frequency, and operating at low temperatures. Fig. 20 shows the torque noise spectrum of a balance operated near the thermal limit. The solid line shows the expected thermal noise limit for $Q = 4000$. (Q was deduced from a separate measurement of the decay of large-amplitude oscillations.) Also shown are data from the same torsion balance operated in electrostatic feedback mode. The low-frequency torque noise agrees with Eq. (57).

Attempts to obtain lower κ/Q values [154] by fabricating fibers from quartz or fused silica (which have intrinsically higher Q's than metals) have not produced significant improvements. As the fibers are made thinner to reduce κ, surface effects reduce Q from the bulk value. In addition, the metallic coating required to make the fiber conducting significantly spoils the Q and mitigates most of the advantages of these materials.

For technical simplicity, most torsion balances have been operated at room temperature. Newman et al. have experimented with a cryogenic torsion balance [36,155]. In principle, cryogenic operation is advantageous, not only because of the reduction in $\sqrt{k_BT}$ but also because of the reduced sensitivity of fiber properties to temperature variations, the ease of temperature control, and because the Q of most materials increases significantly. However, to date cryogenic instruments have not significantly improved on the performance of room-temperature instruments.

6.2.2. Ground vibrations

The coupling of energy from other mechanical modes of the pendulum into the torsional mode can be a serious source of noise. The dominant "parasitic" modes of concern are pendulum swing, rotation of the pendulum body about a horizontal axis ("wobble") and the stretching mode of the torsion fiber resulting in an up–down motion of the pendulum ("bounce"). In a typical torsion balance with a one meter long fiber, the swing, wobble and bounce frequencies, $f_s \approx 0.5$ Hz, $f_w \approx 2$ Hz and $f_b \approx 8$ Hz, are far removed in frequency from the torsional mode $f_0 \approx 1$ mHz. However, the energy content for a 1 μm motion in the swing, wobble and bounce mode exceeds k_BT by many orders of magnitude: $E_s = 10^9 k_BT$, $E_b = 10^{11} k_BT$, so that small imperfections in the suspension system can cause significant energy to leak into the torsional mode. These imperfections can be quite subtle. In very short-range $1/r^2$ tests, the bounce and swing modes are effectively coupled to the torsional mode electrostatically (see Section 6.2.3). In any torsion-balance experiment, dissipation of the bounce mode energy heats the fiber and causes its equilibrium twist to vary (Section 6.4.4). These parasitic modes are excited by ground vibrations and by equipment of the instrument itself. Generally the torsion balances are located in quiet locations and on solid foundations. Roughing pumps are placed some distance away and are vibrationally decoupled through bellows. Most passive, as well as active vibration isolation systems have proven to be impractical as they are not tilt-stable at low frequencies (<100 mHz). Eddy-current dampers from which torsion fibers are suspended have proven effective at damping the parasitic modes of the pendulum while leaving the torsional mode unaffected.

6.2.3. Surface potential fluctuations

In experiments, such as those discussed in Section 3.3, for which small separations (<100 μm) between the pendulum and nearby objects are necessary, fluctuating electric surface potentials are the leading source of noise. A torsion-balance experiment searching for small forces that may act on the LISA proof masses found that the electrostatic potential difference between 50 cm^2-sized Au-coated surfaces ranged up to 100 mV, and the surface potential fluctuations were $\approx 30\ \mu\text{V}/\sqrt{\text{Hz}}$ at 1 mHz [156]. Because the sub-gravitational effects of interest are very weak compared to electrostatic forces, it is important that the pendulum be grounded to avoid charging due to cosmic rays.

6.3. Sensitivity scaling relations

Here, we apply the considerations in Section 6.2.1 to obtain scaling relations for the inherent sensitivity of differential acceleration measurements. If thermal noise (and not readout noise) is the limiting factor, the smallest differential acceleration that can be resolved with a torsion pendulum consisting of two point masses and negligible passive mass, as shown in Fig. 1, is

$$\Delta a(f) = \sqrt{\frac{8k_B T\kappa}{\pi Q m^2 r_{12}^2 f T_{\text{int}}}}, \tag{58}$$

where f is the frequency of the signal and T_{int} denotes the integration time, i.e. the duration of the data set. The torsion constant of a cylindrical fiber is $\kappa = \pi S D^4/32l$, where D and l are the diameter and length of the fiber and S is the shear modulus of the fiber material. The breaking strength of the fiber determines the maximum mass that can be suspended so that $m_{max} = \pi Y D^2/4g$, with Y being the yield strength. Combining these equations yields

$$\Delta a(f) = \sqrt{\frac{4k_B T g}{\pi^2 r_{12}^2 f T_{\text{int}}}}\sqrt{\frac{S}{QY^2 l}}. \tag{59}$$

The second square root contains the fiber properties, and is independent of the fiber diameter, but is strongly dependent on the yield strength. The yield strength of tungsten is the strongest of all metals. (We found a practical breaking strength for a 20 μm diameter tungsten fiber to be about 1.1 N, but we support only 0.7 N to avoid pre-breaking creep.) The equation also indicates that for a given pendulum mass the thinnest fiber that supports the weight should be used. Obviously the passive mass, the suspended material not in test bodies, must be minimized.

The resolvability of differential accelerations scales with the pendulum dimensions, r_{12}, leading one to believe that the size of the torsion pendulum should be maximized. However an increasing pendulum size also leads to increased sensitivity to gravitational gradients. For experiments that use the Sun or the directions to the fixed stars, gravity gradients are less of a concern as the gradients from these sources are negligible. However, in experiments that study local or terrestrial attractors, coupling to local gradients occurs at the same frequency as the signal of interest, forcing one to reduce the size of the pendulum.

The differential acceleration resolvability argument given above assumes that readout noise of the twist-angle sensor angles is well below the angular excursions from the $k_B T$ noise. If readout noise becomes an issue, then the signal frequency must be chosen so that the pendulum harmonic oscillator response does not substantially attenuate the signal (see Ref. [2]).

6.4. False effects

6.4.1. Gravitational coupling

Gravitational coupling discussed in detail in Section 2.2 is a leading source of systematic uncertainty for many torsion balance experiments.

6.4.2. Turntable imperfections

For experiments on turntables, it is important that the rotation be extremely constant, and not introduce excessive vibrations or angular accelerations occurring once per revolution. To discriminate against stable turntable imperfections, the torsion pendulum orientation can be reversed relative to the turntable by rotating the top attachment of the torsion fiber. The stability of turntable imperfections can be determined by monitoring the pendulum deflection at higher harmonics of the turntable frequency.

6.4.3. Electrostatic and magnetostatic effects

Because of electrostatic coupling, all surfaces near the pendulum as well as the pendulum itself must be grounded and coated with a suitable conductor such as gold. In particular, insulated objects in the vicinity of the pendulum should be avoided. Magnetic coupling is minimized by using highly non-magnetic materials, using machining techniques such as electric-discharge milling that cannot introduce magnetic impurities, and by surrounding the pendulum with multiple layers of magnetic shielding. In the EW group's equivalence principle test four layers of spaced μ-metal shields are employed. Because electromagnetic shielding is very effective, electromagnetic effects generally do not lead to large uncertainties. However, is interesting to note that torsion balances are well suited for measuring magnetic impurities in material samples.

6.4.4. Thermal effects

Several mechanisms contribute to the temperature sensitivity of torsion balances. Because of their small diameter to length ratio, torsion fibers are very sensitive to temperature changes. Each time a tungsten torsion fiber is reloaded with the pendulum weight, the fiber displays a slowly varying drift rate (≈ 10 μrad/h). This drift rate can be reduced by heating the entire apparatus to between 50 and 100 °C for one day. After this bakeout, the drift rate is usually <100 nrad/h but still remains a sensitive function of temperature, so that tight control of the temperature is essential. Several other mechanisms, such as thermal expansion and outgassing, convert temperature fluctuations and temperature gradients into a real or apparent pendulum twist. Because of the difficulty of understanding in detail the temperature-twist couplings, it is generally difficult to quantify uncertainties associated with thermal effects, which leads to substantial contributions in the error budget [12].

All delicate torsion balance instruments are located in passive or actively controlled thermal enclosures that are, in turn, located in temperature-controlled rooms. Because of their large surface to volume ratio, radiation rapidly brings torsion fibers into equilibrium with their surroundings. In the EW experiments, the torsion fiber is typically surrounded by a thick thermally isolated copper tube, also in the vacuum. The torsion fiber then adopts the many-hour-long thermal time constant of this tube.

6.4.5. Tilt

When a torsion balance is tipped by a small angle the torsion angle readout registers a deflection. Two mechanisms contribute to this "tilt-twist" effect. Asymmetries at the top attachment of the fiber rotate the fiber. The torsion pendulum responds with a delayed angular deflection as given in Eq. (56). To reduce this coupling, which can be greater than 100%, most torsion fibers are suspended from a pre-hanger–a short section of relatively thick fiber (>75 μm, ≈ 2 cm long). With a pre-hanger, the typical tilt-twist coupling is a few percent. A second, comparable tilt-twist contribution is caused by the displacement of the autocollimator beam with respect to the mirror on the pendulum. This effect is presumably caused by slight curvatures and non-uniform reflectivities of the mirrors. This optical effect is not filtered by the pendulum response and happens without phase delay. Because of the tilt-twist coupling it is imperative that the instrument rotates about the local vertical. Because the level of laboratory floors typically drifts by μrads/day, the tilt coupling must either be understood very well, or the turntable must be continuously leveled. The EW group developed continuous leveling systems for their rotating balances that employ electronic tilt sensors on the rotating instruments. Deviations of the rotation axis from local vertical produce a signal modulated at the rotation rate. A feedback loop changes the length of two of the three support legs of the turntable so that the tilt is zeroed. The length of the support legs is controlled by varying their temperature with Peltier elements. The residual once-per-revolution tilt component at the sensor is nulled to within ± 3 nrad.

Acknowledgements

We acknowledge the contributions of past and present graduate students of the Eöt–Wash group, in particular Todd Wagner and Claire Cramer whose theses constitute some of the unpublished work in this paper. We thank Erik Swanson, Scott Pollack and Charles Hagedorn for help with some of the figures. We are grateful to The National Science Foundation for our primary support via Grant PHY-0653863; additional support comes from the Department of Energy through its support of the Center for Experimental Nuclear Physics and Astrophysics and from NASA grant NNC04GB03G.

References

[1] D.N. Spergel, et al., Astrophys. J. Supp. 170 (2007) 377.
[2] E.G. Adelberger, B.R. Heckel, A.E. Nelson, Ann. Rev. Nucl. Part. Sci. 53 (2003) 77.
[3] B. Bertotti, L. Iess, P. Tortora, Nature 425 (2003) 374.
[4] J.M. Weisberg, J.H. Taylor, arXiv:hep-ph/0407149.
[5] T.D. Lee, C.N. Yang, Phys. Rev. 98 (1955) 1501.
[6] R.D. Peccei, J. Sola, C. Wetterich, Phys. Lett. B 195 (1987) 183.
[7] E.G. Adelberger, et al., Phys. Rev. D 42 (1990) 3267.
[8] S. Baeßler, B.R. Heckel, E.G. Adelberger, J.H. Gundlach, U. Schmidt, H.E. Swanson, Phys. Rev. Lett. 83 (1999) 3585.
[9] P.G. Nelson, D.M. Graham, R.D. Newman, Phys. Rev. D 42 (6) (1990) 93.
[10] G.L. Smith, C.D. Hoyle, J.H. Gundlach, E.G. Adelberger, B.R. Heckel, H.E. Swanson, Phys. Rev. D 61 (2000) 22001.
[11] Y. Su, B.R. Heckel, E.G. Adelberger, J.H. Gundlach, M. Harris, G.L. Smith, H.E. Swanson, Phys. Rev. D 50 (1994) 3614.

[12] S. Schlamminger, K.-Y. Choi, T.A. Wagner, J.H. Gundlach, E.G. Adelberger, Phys. Rev. Lett. 100 (2008) 041101.
[13] M.A. Beilby, R.D. Newman, N. Krishnan, S. Hatamian, Proc. Recontres Moriond (1993) 417.
[14] C.J. Allègre, J.-P. Poirier, E. Humler, A.W. Hofmann, Earth Planet. Sc. Lett. 134 (1995) 515.
[15] C.W. Stubbs, Phys. Rev. Lett. 70 (1993) 119.
[16] E.G. Adelberger, N.A. Collins, C.D. Hoyle, Classical Quantum Gravity 23 (2006) 125; Classical Quantum Gravity 23 (2006) 5643. (corrigendum).
[17] R.v. Eötvös, D. Pekár, E. Fekete, Ann. Phys. 373 (1922) 11.
[18] H.H. Potter, Proc. Roy. Soc. Lond. 104 (1923) 588.
[19] P.G. Roll, R. Krotkov, R.H. Dicke, Ann. Phys. 26 (1964) 442.
[20] V.G. Braginsky, V.I. Panov, JETP 34 (1972) 463.
[21] E. Fischbach, D. Sudarsky, A. Szafer, C. Talmadge, S.H. Aronson, Phys. Rev. Lett. 56 (1986) 3.
[22] F.D. Stacey, G.J. Tuck, G.I. Moore, S.C. Holding, B.D. Goodwin, R. Zhou, Rev. Modern Phys. 59 (1987) 157.
[23] C.W. Stubbs, et al., Phys. Rev. Lett. 58 (1987) 1070.
[24] T.M. Niebauer, M.P. McHugh, J.E. Faller, Phys. Rev. Lett. 59 (1987) 609.
[25] K. Kuroda, N. Mio, Phys. Rev. D 42 (1990) 3903.
[26] R. Cowsik, N. Krishnan, S.N. Tandon, S. Unnikrishnan, Phys. Rev. Lett. 64 (1990) 336.
[27] J.G. Williams, S.G. Turyshev, D.H. Boggs, Phys. Rev. Lett. 93 (2004) 261101.
[28] K. Nordtvedt, Phys. Rev. D 37 (1988) 1070.
[29] B.R. Heckel, Proceedings of the XVIII International Conference on Atomic Physics, 2002, 159.
[30] A.M. Dziewonski, D.L. Anderson, Phys. Earth. Planet. Inter. 25 (1981) 297.
[31] J.W. Morgan, E. Anders, Proc. Natl. Acad. Sci. 77 (1980) 6973.
[32] T.A. Wagner, Ph.D. Thesis, University of Washington (in press).
[33] C. Talmadge, J.-P. Berthias, R.W. Hellings, E.M. Standish, Phys. Rev. Lett. 61 (1159) (1988).
[34] S.G. Turyshev, J.G. Williams, Internat. J. Modern Phys. D 16 (2007) 2165.
[35] T.W. Murphy Jr., et al., Pub. Astr. Soc. Pacific 20 (2008) 20.
[36] M.K. Bantel, R.D. Newman, J. Alloys Compounds 310 (2000) 233.
[37] R.D. Reasenberg, J.D. Phillips, in: V. Alan Kostelecky (Ed.), Proceedings of the Fourth Meeting on CPT and Lorentz Symmetry, World Scientific, New Jersey, 2008. see also: http://cfa-www.harvard.edu/poem/docs/Proposals/TechnicalP6691-6-07.pdf.
[38] P. Worden, Ph.D. Thesis, Stanford University, 1976.
[39] P. Worden, R. Torii, J.C. Mester, C.W.F. Everitt, Adv. Space Res. 25 (2000) 1205.
[40] P. Touboul, M. Rodrigues, Class. Quantum Grav. 18 (2001). 2487. see also: http://microscope.onera.fr/mission.html.
[41] A.M. Nobili, D. Bramanti, E. Polacco, I.W. Roxburgh, G. Comandi, G. Catastini, Classical Quantum Gravity 17 (2000) 2347.
[42] A.J. Sanders, et al., Meas. Sci. Technol. 10 (1999) 514.
[43] G.G. Raffelt, Stars as Laboratories for Fundamental Physics, Univ. of Chicago Press, 1996.
[44] J. Sucher, G. Feinberg, in: F.S. Levin, D.A. Micha (Eds.), Long-Range Casimir Forces, Plenum, New York, 1993, pp. 273–348.
[45] F. Ferrer, J.A. Grifols, Phys. Rev. D 58 (1998) 096006.
[46] G. Feinberg, J. Sucher, Phys. Rev. 166 (1968) 1638.
[47] N.G. Deshpande, S.D.H. Hsu, J. Jiang, arXiv:0708.2735v2.
[48] N. Arkani-Hamed, S. Dimopoulis, G.R. Dvali, Phys. Lett. B 436 (1998) 257.
[49] G. Dvali, G. Gabadadze, M. Kolanović, F. Nitti, Phys. Rev. D 65 (2001) 024031.
[50] A.G. Riess, et al., Astron. J. 116 (1998) 1009.
[51] S. Perlmutter, et al., Astrophys. J. 517 (1999) 565.
[52] S.R. Beane, Gen. Rel. Grav. 29 (1997) 945.
[53] R. Sundrum, Phys. Rev. D 69 (2004) 044014.
[54] J. Khoury, A. Weltman, Phys. Rev. Lett. 93 (2004) 171104.
[55] A. Upadhye, S.S. Gubser, J. Khoury, 2006. hep-ph/0608186.
[56] B. Feldman, A.E. Nelson, 2006. hep-ph/060307.
[57] D.F. Mota, D.J. Shaw, Phys. Rev. Lett. 97 (151102) (2006).
[58] H. Georgi, Phys. Rev. Lett. 98 (2007) 221601.
[59] L.-G. Tu, S.-G. Guan, J. Luo, C.-G. Shao, L.-X. Liu, Phys. Rev. Lett. 98 (2007) 201101.
[60] C.D. Hoyle, et al., Phys. Rev. Lett. 86 (2001) 1418.
[61] C.D. Hoyle, et al., Phys. Rev. D 70 (2004) 042004.
[62] D.J. Kapner, et al., Phys. Rev. Lett. 98 (2007) 021101.
[63] C.C. Speake, Classical Quantum Gravity 13 (1996) A291.
[64] H.B. Michaelson, J. Appl. Phys. 48 (1977) 4729.
[65] L. Deslauriers, et al., Phys. Rev. Lett. 97 (2006) 103007.
[66] J. Labaziewicz, et al., Phys. Rev. Lett. 100 (2008) 013001.
[67] R.S. Decca, et al., J. Low Temp. Phys. 135 (2004) 63.
[68] W. Westphal, H. Abele, S. Baeßler, 2007. hep-ph/0703108.
[69] R. Spero, et al., Phys. Rev. Lett. 44 (1980) 1645.
[70] J.K. Hoskins, et al., Phys. Rev. D 32 (1985) 3084.
[71] J.C. Long, et al., Nature 421 (2003) 922.
[72] J. Chiaverini, et al., Phys. Rev. Lett. 90 (2003) 151101.
[73] S.J. Smullin, et al., Phys. Rev. D 72 (2005) 122001.
[74] M.V. Moody, H.-J. Paik, Phys. Rev. Lett. 70 (1993) 1195.
[75] E.G. Adelberger, et al., Phys. Rev. Lett. 98 (2007) 131104.
[76] E. Fischbach, D.E. Krause, Phys. Rev. Lett. 83 (1999) 3593.
[77] F. Ferrer, M. Nowakowski, Phys. Rev. D 59 (1999) 075009.
[78] E.G. Adelberger, E. Fischbach, D.E. Krause, R.D. Newman, Phys. Rev. D 68 (2003) 062002.
[79] G. Raffelt, hep-ph/0611118.
[80] D. Colladay, V.A. Kostelecký, Phys. Rev. D 55 (1997) 6760; Phys. Rev. D 58 (1998) 116002; V.A. Kostelecký, Phys. Rev. D 69 (2004) 105009.
[81] V.A. Kostelecký, N. Russell, 2008. arXiv:0801.0287.
[82] R. Bluhm, V.A. Kostelecký, Phys. Rev. Lett. 84 (2000) 1381.
[83] N. Arkani-Hamed, et al., J. High Energy Phys. 0405 (2004) 074.
[84] H.-C. Cheng, M.A. Luty, S. Mukohyama, J. Thaler, J. High Energy Phys. 0605 (2006) 076.
[85] Jesse Thaler, private communication.
[86] Claire Cramer, Ph.D. Thesis, University of Washington, unpublished, 2007.
[87] S.M. Carroll, J.A. Harvey, V.A. Kostelecký, C.D. Lane, T. Okamoto, Phys. Rev. Lett. 87 (2001) 141601.
[88] I. Hinchliffe, N. Kersting, Y.L. Ma, Internat. J. Modern Phys. A 19 (2004) 179. hep-ph/0205040.
[89] A. Ansimov, T. Banks, M. Dine, M. Graesser, Phys. Rev. D 65 (2002). 085032. hep-ph/0106356.
[90] J.E. Moody, F. Wilczek, Phys. Rev. D 30 (1984) 130.

[91] B.A. Dobrescu, I. Mocioiu, J. High Energy Phys. 0611 (2006) 5. hep-ph/0605342.
[92] I.L. Shapiro, Phys. Rep. 357 (2002) 113.
[93] C. Lämmerzahl, Phys. Lett. A 228 (1997) 233.
[94] V.A. Kostelecký, N. Russell, J.D. Tasson, 2007. arXiv:0712.4393.
[95] R.T. Hammond, Phys. Rev. D 52 (1995) 6918.
[96] F. Canè, et al., Phys. Rev. Lett. 93 (2004) 230801.
[97] M. Pospelov, M. Romalis, Phys. Today 40 (2004).
[98] W.T. Ni, et al., Phys. Rev. Lett. 82 (1999) 2439.
[99] R.P. Phillips, Phys. Rev. Lett. 59 (1987) 1784.
[100] L.-S. Hou, W.-T. Ni, Y.-C. Li, Phys. Rev. Lett. 90 (2003) 201101-1.
[101] B.R. Heckel, et al., Phys. Rev. Lett. 97 (2006) 021603.
[102] B.R. Heckel, et al. Phys. Rev. D (submitted for publication).
[103] D. Givord, J. Laforest, J. Schweizer, F. Tasset, J. Appl. Phys. 50 (1979) 2008.
[104] P. Tils, M. Loewenhaupt, K.H.J. Buschow, R.S. Eccleston, J. Alloys Compounds 289 (1999) 28.
[105] A. Koizumi, N. Sakai, N. Shirai, M. Ando, J. Phys. Soc. Japan 66 (1997) 318.
[106] A.N. Youdin, et al., Phys. Rev. Lett. 77 (1996) 2170.
[107] D.J. Wineland, et al., Phys. Rev. Lett. 67 (1991) 1735.
[108] F. Wilczek, Phys. Rev. Lett. 49 (1982) 1549.
[109] Y. Chikashige, R.N. Mohapatra, R.D. Peccei, Phys. Lett. B 98 (1981) 265.
[110] G.B. Gelmini, M. Roncadelli, Phys. Lett. B 99 (1981) 411.
[111] A.A. Anselm, N.G. Uraltsev, Phys. Lett. B 114 (1982) 39.
[112] P. Sikivie, Phys. Rev. Lett. 61 (1988) 783.
[113] S. Weinberg, Phys. Rev. Lett. 40 (1978) 223.
[114] F. Wilczek, Phys. Rev. Lett. 40 (1978) 279.
[115] H. Davoudiasl, Phys. Lett. B 646 (2007) 172.
[116] P. Svrcek, E. Witten, JHEP 0606 (2006) 051.
[117] K.-S. Choi, I.-W. Kim, J.E. Kim, JHEP 0703 (2007) 116.
[118] K.R. Dienes, E. Dudas, T. Gherghetta, Phys. Rev. D 62 (2000) 105023.
[119] S. Chang, S. Tazawa, M. Yamaguchi, Phys. Rev. D 61 (2000) 084005.
[120] R.D. Peccei, H. Quinn, Phys. Rev. Lett. 38 (1977) 1440.
[121] R.D. Peccei, H. Quinn, Phys. Rev. D 16 (1977) 1791.
[122] M. Pospelov, A. Ritz, Phys. Rev. Lett. 83 (1999) 2526.
[123] C.A. Baker, et al., Phys. Rev. Lett. 97 (2006) 131801.
[124] M.V. Romalis, W.C. Griffith, J.P. Jacobs, E.N. Fortson, Phys. Rev. Lett. 86 (2001) 2505.
[125] J.E. Kim, Phys. Rev. Lett. 43 (1979) 103;
M.A. Shifman, A.I. Vainstein, V.I. Zakharov, Nuclear Phys. B 166 (1980) 493.
[126] M. Dine, W. Fischler, M. Srednicki, Phys. Lett. B 104 (1981) 199;
A.R. Zhitnitsky, Sov. J. Nucl. Phys. 31 (1980) 260.
[127] W.-M. Yao, et al., Particle Data Group J. Phys. G 33 (2006) 1. and 2007 partial update for edition 2008 (URL: http://pdg.lbl.gov).
[128] W.A. Bardeen, R.D. Peccei, T. Yanagida, Nuclear Phys. B 279 (1987) 401;
Adler, et al., Phys. Rev. Lett. 88 (2002) 041803.
[129] M. Beltrán, J. García-Bellido, J. Lesgourgues, Phys. Rev. D 75 (2007) 103507.
[130] P. Sikivie, Lect. Notes Phys. 741 (2008) 19.
[131] G.G. Raffelt, Lect. Notes Phys. 741 (2008) 51.
[132] S. Asztalos, et al., Phys. Rev. D 69 (2004) 011101.
[133] L. Duffy, et al., Phys. Rev. Lett. 95 (2005) 091304.
[134] E.P.S. Shellard, R.A. Battye, Phys. Rep. 307 (1998) 227.
[135] R.A. Battye, E.P.S. Shellard. arXiv:astro-ph/9909231v1.
[136] S.L. Cheng, C.Q. Geng, W.T. Ni, PRD 52 (1995) 3132.
[137] S. Andriamonje, et al., J. Cosm. Astroparticle Phys. 04 (2007) 010.
[138] E. Zavattini, et al., Phys. Rev. Lett. 96 (2006) 110406.
[139] E. Zavattini, et al., Phys. Rev. D 77 (2008) 032006.
[140] C. Robilliard, et al., Phys. Rev. Lett. 99 (2007) 190403;
A.S. Chou, et al., Phys. Rev. Lett. 100 (2008) 080402;
P. Pugnat, et al. arXiv:0712.3362v1[hep-ex].
[141] S. Baeßler, et al., Phys. Rev. D 75 (2007) 075006.
[142] B.J. Venema, et al., Phys. Rev. Lett. 68 (1992) 135.
[143] G.D. Hammond, et al., Phys. Rev. Lett. 98 (2007) 081101; Phys. Rev. D 77 (2008) 036005.
[144] S. Hoedl, F. Fleischer, B.R. Heckel, E.G. Adelberger, in press.
[145] G.L. Smith, C.D. Hoyle, J.H. Gundlach, E.G. Adelberger, B.R. Heckel, H.E. Swanson, Phys. Rev. D 61 (1999) 022001.
[146] T.J. Quinn, C.C. Speake, S.J. Richman, R.S. Davis, A. Picard, Phys. Rev. Lett. 87 (2001) 111101.
[147] M.W. Moore, A. Boudreaux, M. DePue, J. Guthrie, R. Legere, A. Yan, P.W. Boynton, Classical Quantum Gravity 11 (1994) A97.
[148] R. Cowsik, R. Srinivasan, S. Kasturirengan, A. Senthil Kumar, K. Wagoner, Rev. Sci. Instrum. 78 (2007) 035105.
[149] R.D. Rose, et al., Phys. Rev. Lett. 23 (1969) 665.
[150] J.H. Gundlach, S. Merkowitz, Phys. Rev. Lett. 85 (2000) 2869.
[151] E.C. Berg, et al. Proceedings of the 10th Marcel Grossman Conference. arXiv:gr-qc/0403021v2, 2003.
[152] S. Pollack, private communication, 2008.
[153] P.R. Saulson, Phys. Rev. D 42 (1990) 2437.
[154] C. Hagedorn, S. Schlamminger, J.H. Gundlach, AIP Conf. Proc. 873 (2006) 189.
[155] R. Newman, Classical Quantum Gravity 18 (2001) 2407.
[156] S. Pollack, S. Schlamminger, J.H. Gundlach, in press.